Spacecraft Geometry Effects on Kinetic Impactor Missions

J. Michael Owen[1] , Mallory E. DeCoster[2] , Dawn M. Graninger[2] , and Sabina D. Raducan[3]
[1] Lawrence Livermore National Laboratory, M/S L-38, Livermore, CA 94550, USA; mikeowen@llnl.gov
[2] The Johns Hopkins University Applied Physics Laboratory, Laurel, MD 20723, USA
[3] Space Research and Planetary Sciences, Physikalisches Institut, University of Bern, Switzerland

Abstract

The DART (Double Asteroid Redirection Test) mission will impact a spacecraft on the secondary (Dimorphos) of the binary asteroid system Didymos in 2022 September, with the goal of altering the orbital period of Dimorphos about Didymos sufficiently to be observed from ground-based observations. Numerical impact modeling is a crucial component in understanding the outcome of the DART experiment, and while many have investigated the effects of target properties, such as material strength and porosity (which remain unknown), an often overlooked factor is the importance of accurately representing the spacecraft itself in such models. Most impact modeling to date has considered simple impactor geometries such as a solid uniform sphere, but in reality the spacecraft is a complex shape full of different components, open spaces, and thin walled structures. At a minimum, a simple solid representation underestimates the surface area of the impact: for a small body such as Dimorphos (approximately 160 m in diameter), the difference between a spacecraft spanning 20 m (including solar arrays) impacting and a sub-1 m idealized shape may be important. In this paper, we compare models impacting high-fidelity models of the spacecraft based on the CAD geometry with various simplified impactors, in order to assess the potential importance of this effect. We find that the difference between the simplest impactor geometries (such as a uniform sphere) and the real spacecraft is measurable, and has an interesting dependence on the material properties of the asteroid itself.

Unified Astronomy Thesaurus concepts: Impact phenomena (779); Planetary science (1255); Asteroids (72); Space vehicles (1549)

1. Introduction

In the event of a potentially hazardous asteroid (PHA) approaching Earth, diverting it using a kinetic impactor mission is one of our first lines of defense. A kinetic impactor is a spacecraft that impacts the asteroid, thereby directly transferring momentum to the target and altering its orbital path. Any ejecta launched from the impact site will, by conservation of momentum, increase the effective momentum delivered to the asteroid, resulting in a larger deflection velocity (Housen & Holsapple 2012). Understanding this cratering and ejecta formation is a critical component of understanding how practical a kinetic impactor might be as a tool for deflecting asteroids. The amount of momentum enhancement ejecta produces during an impact is difficult to estimate a priori. Estimates range from near zero to many times the momentum of the spacecraft itself, a wide range dominated by uncertainties in many variables: the material properties of the asteroid (porosity, yield strength, etc.) (Jutzi & Michel 2014; Stickle et al. 2015; Bruck Syal et al. 2016; Stickle et al. 2017; Raducan et al. 2019); the local slope of the terrain at the impact point (Bruck Syal et al. 2016); the structure of the asteroid near the impact site (Graninger et al. 2018; Raducan et al. 2020); etc. Given all the complications and the wide range of predictions to date, experimental data to restrict these unknown outcomes are needed.

The NASA DART mission (Double Asteroid Redirection Test; Cheng et al. (2018)) will be the first full-scale test of a kinetic impactor. The DART spacecraft will impact the secondary (Dimorphos) in the binary asteroid system (65803) Didymos in 2022 September, with the goal of changing the orbital period of Dimorphos around the primary sufficiently to be measured by ground-based observations. This will provide the first experimental value for the deflection velocity of an asteroid due to a kinetic impactor. Additionally, DART is carrying a cubesat mission, LICIACube (Light Italian Cubesat for Imaging of Asteroids; Dotto et al. (2021)), which will observe the impact and the early stages of the ejecta plume. LICIACube will be released from DART 10 days before impact, and maneuver so that it will flyby Dimorphos (closest approach ∼55 km) a few minutes behind DART. This will allow LICIACube to observe the impact and a few minutes of the ejecta formation, as well as capture more of Dimorphos' shape (important for reconstructing the volume and mass of Dimorphos). Following the DART mission, the ESA (European Space Agency) Hera mission (Michel et al. 2018) will rendezvous with the Didymos system several years after the DART impact, and offers the opportunity to study the system in much greater detail, including characterizing the crater created by DART.

As outlined above, the unknown material and structural properties of Dimorphos result in large uncertainties for the ejecta properties and resulting deflection from the DART mission. However, another little-studied variable that could affect the outcome of the DART impact is the geometry of the impactor itself. Much of our understanding of how the crater and associated ejecta evolve comes from either numerical modeling of idealizations of the impact and reaction of the target material, or laboratory-scale experiments that also rely on highly simplified impactor geometries. There have been some

investigations of the effect of projectile geometry. Ikeda et al. (2017) performed a series of gas gun experiments with projectiles with different simple shapes (cylinders, spheres, cones, and cups). Of particular relevance to our study, Ikeda et al. (2017) note a complex trend in the resulting ejecta momentum based on projectile type and impact velocity: hollow shapes produce larger ejecta momenta for small impact velocities, while a solid sphere impactor fares best at high impact velocities. Hermalyn et al. (2012) employed a gas gun to fire solid and hollow aluminum spheres into both sandy material and a pumice-like dust in order to understand the results of another impact using a man-made impactor: the LCROSS (Lunar Crater Observation and Sensing Satellite) experiment, wherein a hollow Centaur rocket body impacted the lunar surface. In these experiments, the hollow impactors fail early in the impact and allow material to escape from the interior of the crater (inside the traditional ejecta curtain), representing a separate high-angle ejecta plume. On the numerical modeling side, Shuvalov & Trubetskaya (2008) and Korycansky et al. (2009) present a variety of calculations for the LCROSS experiment. Shuvalov & Trubetskaya (2008) compare impacts using solid and hollow impactors, while Korycansky et al. (2009) examine cases with either a solid low-density impactor or impactors consisting of parallel plates (to mock up a hollow rocket body). Both find there are distinctions in the ejecta produced due to the projectile geometry. In a companion study to this paper, Raducan et al. (2022) examine a series of models using solid and hollow impactors in various configurations using the iSALE code in 2D, along with one elongated rod-like impactor model in 3D impacting with the long axis parallel to the surface. This study finds minimal differences comparing hollow and solid structures with similar extents, but does note a larger distinction in the crater and ejecta when comparing the elongated rod with a spherical impactor.

These numerical and experimental studies suggest the relationship between impactor shape, ejecta formation, and momentum transfer is not straightforward, even for simple impactor geometries. For more complicated impactor shapes, such as the DART spacecraft, simulations generally assume an idealized solid metal shape for the impactor (typically a sphere, cube, or cylinder) using the same mass as the spacecraft, and as a first approximation this is perfectly reasonable. However, based on the sensitivity to impactor shape for simple geometries found in these prior studies, it is possible that this simplification may influence the deflection at some level of detail. The DART spacecraft has a central bus housing most of the electronics, thrusters, tanks, antenna, and so forth in roughly a $1.8\,\mathrm{m} \times 1.9\,\mathrm{m} \times 2.6\,\mathrm{m}$ volume, while the ROSA (Roll Out Solar Arrays) solar panels are over 8.5 m long when extended (and represent $\sim$16% of the spacecraft mass). If we represent all of this DART material (totaling approximately 535 kg dry mass) as a single solid aluminum sphere, we get a sphere just over 70 cm in diameter, representing a very different mass distribution and effective surface area on impact. The effect of simplifying the impactor geometry may become more important as the impactor size becomes non-negligible compared with that of the target. DART is $\sim$20 m along the longest axis (aligned with the solar arrays), and Dimorphos is estimated to be roughly 160 m in diameter. Among all the unknowns about a kinetic impactor mission (most involving the target asteroid), the elements we will know with the most

Table 1
DART Spacecraft Mass Per Material

Material	Mass (kg)
Aluminum	436.57
Ti-6Al-4V alloy	54.43
Stainless steel	22.40
Silicon	21.60
Total	535

certainty are the properties of the spacecraft itself. In this paper, we examine what sort of effect different representations of the impactor might have on our predictions of the DART impact using numerical simulations, up to high-fidelity CAD models of the full spacecraft geometry.

2. Models

In this study, we compare the results from three different codes spanning a range of numerical methodologies: CTH, using mesh-based Eulerian adaptive mesh refinement (AMR) (McGlaun et al. 1990; Crawford 1999); iSALE, another mesh-based Eulerian approach (Amsden et al. 1980; Wünnemann et al. 2006; Collins et al. 2011); and Spheral, a mesh-free Lagrangian Adaptive Smoothed Particle Hydrodynamics (ASPH) code (Owen et al. 1998; Owen 2010, 2014). An overview of these codes applied to impact relevant test problems in preparation for the DART mission is available in Stickle et al. (2020). We note that, in this study we are only considering the short-timescale (less than a second or two) shock hydrodynamic response of the material and formation of the fastest ejecta and transient crater, and therefore gravitational interactions of this material with Dimorphos/Didymos are negligible and not modeled.

In order to create our model of the DART impactor, we start with a simplification that captures the major components (panels, electronics boxes, tanks, antennae, etc.) in individual STL files from the spacecraft design CAD model. These are made up of four different materials (listed in Table 1), and are distributed between the central bus (459.7 kg) and solar arrays (37.65 kg each), for a total of 535 kg dry mass (excluding fuel). This representation is a compromise: we capture the major structural features that are the most likely to be relevant to the impact (component boxes, panels, tanks, open spaces, etc.), while dropping the finest features such as connectors, wires, and assorted small electronic components that fall below our effective resolution of a few centimeters in the spacecraft. Figure 1 compares the input CAD geometry and the simulated realization as generated in Spheral and CTH: note that, in this view, you can see the NEXT-C (NASA's Evolutionary Xenon Thruster) thruster on top of the bus, the high-gain antenna on the right-side corner of the bus, and the strut, roller, and panel structures of the ROSA (Roll Out Solar Arrays) solar panel arrays. Although it is not visible in Figure 1, the central bus includes the open spaces from the hollow tanks, electrical boxes, and panels that make up the structure of the central bus —see Cheng et al. (2018) for more discussion of the spacecraft. On impact, we expect the DRACO (Didymos Reconnaissance and Asteroid Camera for Optical navigation) camera (on the bottom in Figure 1) to be leading, while the NEXT-C ion thruster would be on the trailing side of the spacecraft. We have also rotated the ROSA panels so they are parallel with the impact plane in this example.

| (a) CAD input | (b) Spheral | (c) CTH |
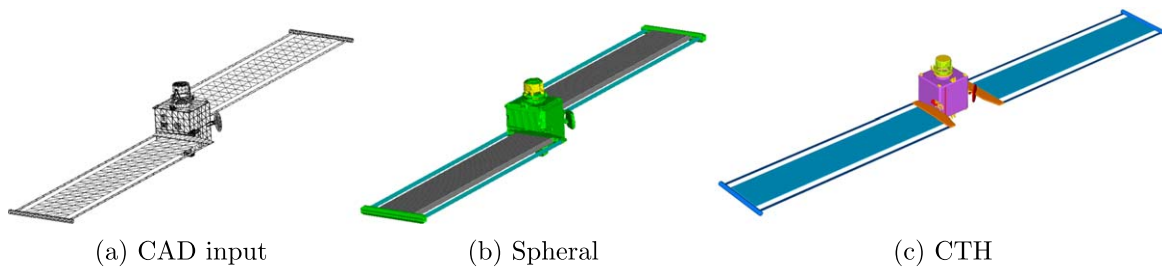
Figure 1. DART spacecraft geometry initial conditions. The left panel shows the input CAD geometry for the spacecraft, the middle panel shows the polyhedral Voronoi reconstruction of the ASPH nodes in the Spheral (colored by material), and the right panel shows the CTH materials.

We consider 10 different scenarios for the geometry of impact, depicted in Figure 2 as slices in the (y,z) plane through the initial conditions. These impactor models break into four categories, corresponding to the rows in Figure 2:

DART: The DART spacecraft CAD model. We consider three orientations (0°, 45°, and 90°) with respect to the tangent surface plane of Dimorphos at the impact site, as shown in the top row of Figure 2.

Cylinders: Solid Al cylinders, impacting along the axis of the cylinder. We consider three configurations for these cylinders specified by their diameter D, which, combined with the specified mass and density, fixes the height h: $D = [150, 100, 50]$ cm, corresponding to heights of $h = [11.21, 25.23, 100.92]$ cm, respectively. This gives us cylindrical configurations ranging from a thin plate to a rod.

Three spheres: A set of "three-sphere" configurations, consisting of a central solid Al sphere with a mass equal to that of the spacecraft bus, with two smaller solid Al spheres on either side each with the mass of a spacecraft solar array. Each side sphere is spaced one-quarter the length of a solar array from the central sphere (center to center), or 2.215 m. The central sphere is 459.7 kg (radius 34.38 cm), while each side sphere is 37.65 kg (radius 14.93 cm). As in the full DART CAD models, we consider three orientations for the line of spheres with respect the surface plane: 0°, 45°, and 90°.

Sphere: A solid, uniform Al sphere—given the reference density of Al $(2.7 \, \mathrm{g \, cm^{-3}})$ and the total DART mass (535 kg) yields a radius of 36.16 cm for the sphere.

Note that not all scenarios are modeled in all codes; see the code-specific descriptions in Sections 2.1–2.3 for more details, as well as Table 5 for an overview of which models were run and their final deflection velocities.

In all cases, we enforce the same total impactor mass (535 kg) and impact velocity $(6.65 \, \mathrm{km \, s^{-1}})$, impacting the Dimorphos surface along the z-axis (in a frame where the spherical Dimorphos target is centered at the origin). The first three full DART models (top row of Figure 2) represent our highest-fidelity approximations to model the DART geometry on impact, with orientations spanning the extreme possible cases from face-on (0°) with solar panels spread as far as possible across the initial surface, to end-on (90°), wherein the spacecraft presents the smallest possible surface area on impact. The cylinder geometries (second row of Figure 2) are intended to test how important the impact surface area is in the outcome with an idealized geometry: a cylinder impacting face-on, spanning cases from a thin disk $(D = 150 \, \mathrm{cm})$ to an elongated rod $(D = 50 \, \mathrm{cm})$. The "three-sphere" configuration is a step up

in complexity, with separate spheres for the central bus and solar arrays. These represent a simplified multiple-impactor representation of the DART event, with orientations similar (with respect to the surface of Dimorphos) to those we are considering with the full DART geometry.

Spectroscopic observations (De León et al. 2010) find Didymos to be primarily made from silicate material, so for simplicity we model Dimorphos as a 160 m diameter monolithic sphere of SiO_2. Almost certainly Dimorphos is a porous body, though the mass and porosity remain unknown. We assume a uniform microporosity of 30% for Dimorphos, which is conservatively within the expected range of porosity for a body such as Didymos (Britt et al. 2002; Barnouin et al. 2019; Naidu et al. 2020). The solid density of SiO_2 is $2.65 \, \mathrm{g \, cm^{-3}}$, giving us a bulk density of $1.86 \, \mathrm{g \, cm^{-3}}$ in our idealized representation. The material strength of Dimorphos is unknown, so we model two scenarios: a "strong" case (with solid/damaged yield strengths of 100 MPa and 0.1 MPa) and a "weak" case (solid/damaged yield strengths 0.1 MPa and 0.01 MPa)—see Equations (A3)–(A5) for an explanation of these terms. The full material parameters and numerical implementations of the material models are discussed in the Appendix. Our strong limit is intended to represent competent rock (such as a boulder that might be observed on Earth), while the weak limit is closer to loosely cohesive granular or regolith-like material. Based on recent observations from the OSIRIS-REx (Lauretta et al. 2017) and Hyabusa2 (Arakawa et al. 2020) missions, even weaker cohesion than considered here is possible for the surface material, but for our purposes it is interesting to consider how the effect of changing the projectile geometry may change in these different representative strength regimes.

In the next sections, we discuss the details of each simulation code as they are applied to these scenarios. But before we get into those details, we should discuss the complications of comparing results from multiple codes in this manner. Our goal is to study the effect of the spacecraft geometry using the "best" possible representation of the same scenarios in each code. Because the codes are quite different (both in modeling algorithms as well as the physics incorporated in their individual material models), the "best" possible material representation will vary from code to code, which will exacerbate inter-code differences. If our goal were to get the best possible agreement between the codes, we would fall back to the most common possible material models between them, which are usually the most simplified. Those sorts of validation exercises are extremely valuable, and we present such a comparative study of these codes in Stickle et al. (2020). In that benchmarking study, we find that we can expect, for simplified material models in the strong material limit, agreement to approximately 15% across the codes in metrics such as the
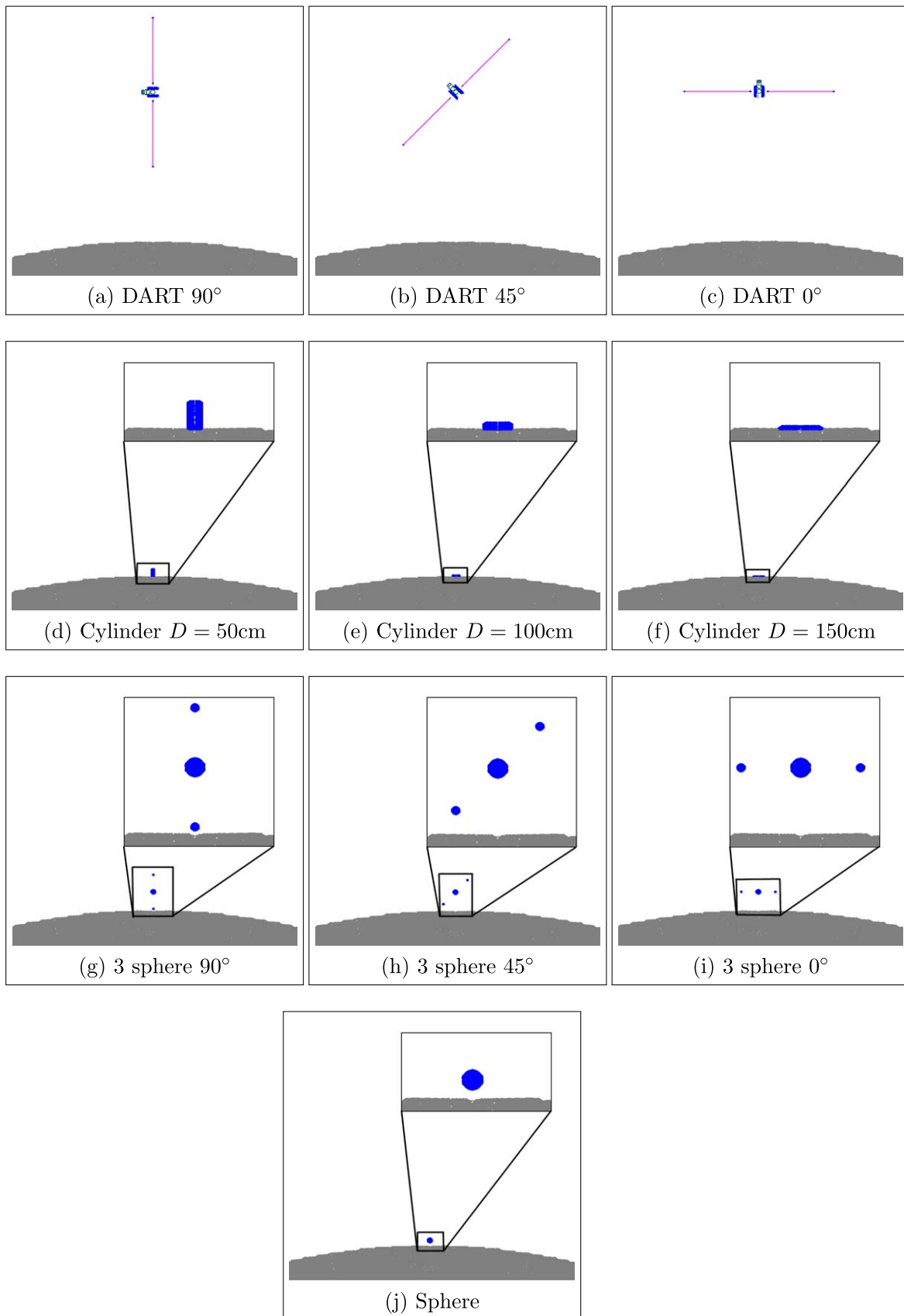
Figure 2. (y, z) plane slices through the initial conditions for our various impactor geometries. The insets for the non-DART scenarios are zoomed-in because those impactors are much smaller than the actual DART geometry.

momentum imparted to the target and crater geometries. In this work, however, our primary goal is fidelity in the results in order to best understand any effect from the projectile geometry, and so we are employing more sophisticated (and varied) material models across the codes. We strive to choose parameters for the models (in particular, material strength and porosity models, which seem the most important in this impact regime) that should lead to consistent material responses, but we do not know a priori whether the outcomes will always agree to the same degree in the absolute metrics as we found in Stickle et al. (2020). Of more importance for this study is how well the codes agree on the trends as we change the impactor geometry, so we focus on that kind of comparison. The following sections (Sections 2.1–2.3) discuss the codes in more detail, while Appendices A.1–A.3 delve into the specifics of the material models employed in each code.

2.1. Spheral Simulations

Spheral is an Adaptive Smoothed Particle Hydrodynamics (ASPH) modeling code (Owen et al. 1998; Owen 2010, 2014). ASPH is a mesh-free Lagrangian method, wherein the material mass in the problem is discretized into a set of points or ASPH nodes that move freely according the Lagrangian evolution equations. Spheral is used to model all 20 of the geometry/material scenarios: 10 geometric representations of the impactor ×2 different material assumptions about Dimorphos' strength parameters. All Spheral simulations presented here are 3D, modeling the entire domain (no boundary conditions). We find it necessary to model the entirety of Dimorphos because the timescale required to follow the crater and ejecta evolution is long enough that sound waves have time to propagate across Dimorphos several times (a single crossing time is on the order of 0.3 sec for the assumed size of Dimorphos). Dimorphos is modeled as a 160 m diameter uniform porous sphere centered at the origin, with the projectile impacting along the z-axis (yielding an impact velocity (0, 0, -6.65 km s^{-1})). In order to make the problem tractable, we do not use a uniform resolution—we require high resolution near the impact site both because of the necessity to model the ejecta with reasonable fidelity and because capturing the DART geometry requires fairly fine resolution. Therefore, we lay down the ASPH points modeling Dimorphos with a starting resolution of 5 cm at the impact point ((0, 0, 80 m) in simulation coordinates), and expand out in spherical shells from that position, increasing the spacing by a ratio of 1.01 for each shell of points (removing any points that are not inside the Dimorphos surface). This approach allows us to establish fine resolution in the impact region, where it is important, and use progressively coarser resolution in the bulk of Dimorphos, which is sufficient for the propagation of signals emerging from the impact zone and reflecting back. As an example of this gradual coarsening in resolution, our starting resolution of 5 cm at the impact point becomes ~15 cm at a radius of 10 m, demonstrating good resolution in a 20 m diameter sphere centered at the impact site, with nearly 3×10^6 SPH points contained in that region. We strive to mass-match the points in the impactor to the point masses at the impact point on Dimorphos as much as possible. For the idealized impactors (spheres and cylinders), this is easily achieved, but in the high-fidelity DART spacecraft models, we have to use finer points in some components (the solar arrays in particular) in order to ensure they are represented reasonably (i.e., points are not

Table 2
Spheral ASPH Node Counts

Object	Number of points
Dimorphos	8,295,072
DART CAD model	19,057
Cylinder ($D = 150$ cm)	1,252
Cylinder ($D = 100$ cm)	1,540
Cylinder ($D = 50$ cm)	1,540
Three-sphere (central sphere)	6,198
Three-sphere (side sphere)	508
Sphere	7,206

Note. The number of ASPH nodes used to model each object in the Spheral models, chosen to match 5 cm resolution (node spacing) at the impact point.

spaced too coarsely). Table 2 lists our node counts per object in the Spheral models; the number of points required for the DART CAD impactor representation is higher than for the other impactors, in order to maintain this spatial fidelity, which forces the compromise of having some lower-mass ASPH points in the DART model than is ideal.

It is worth pointing out that, without the ratioed resolution approach to Dimorphos, it would require $\sim 1.7 \times 10^{10}$ ASPH points to uniformly resolve Dimorphos at a fixed resolution of 5 cm, rather than the $\sim 8 \times 10^6$ points we use here. However, variable resolution like this involves other complications and trade-offs. In many ways, this sort of varying resolution is akin to introducing variable resolution in methods such as Adaptive Mesh Refinement (AMR), familiar to many in the meshed Eulerian modeling community. In this case, however, the resolution remains fixed once initialized, and expands/contracts as normal in response to Lagrangian deformation during the problem evolution. Additionally, this sort of ratioed resolution, which varies smoothly (changing linear resolution by 1% between adjacent points) is much less dramatic than the typical 2× resolution jumps seen at AMR refinement boundaries, and so has less effect on the problem. At all times, exact conservation of mass, momentum, and energy is rigorously maintained. Another complication is that the standard Benz–Asphaug damage model (Benz & Asphaug 1994, 1995), typically used in SPH models in order to follow material fracture and failure, implicitly assumes a uniform resolution in the material, and is not applicable in combination with this sort of ratioed node resolution. For this and other reasons, Spheral employs a generalization of the standard Benz–Asphaug damage model that handles nonuniform resolution. The details of this particular model are beyond the scope of this paper, and will be presented in another publication.

Our primary diagnostics of interest are related to the ejecta. In order to characterize the ejecta from the impacts in the Spheral models, we establish a computational plane 50 cm above the surface at the impact point, and count any material lofted above this plane with $v^z > 5$ cm s^{-1} (a rough estimate of escape velocity) as ejecta. This choice of 50 cm is a compromise: it is high enough to avoid the transient crater lip material, but we try to make it as low as possible in order to capture slow ejecta as it rises from the surface without requiring too much simulation time.

In order to examine the crater evolution, we employ an automated crater fitting method that picks a density isosurface from the surface surrounding the impact point and fits a

Table 3
CTH Simulation and Projectile Geometries

Projectile	Model Coordinates	Dimension (s) (cm)	Mass (kg)	Material (s)
DART (0°)	(x, y, z)	CAD Geometry	535	Various (see Table 1)
Sphere	(x, y, z)	$R = 36.17$	548	Al
Cylinder	(r, z)	$D = 150, h = 11.2$	531	Al
Cylinder	(r, z)	$D = 100, h = 25$	531	Al
Cylinder	(r, z)	$D = 50, h = 100$	531	Al
Three-sphere (90°)	(r, z)	$D_{panel} = 20.67, D_{center} = 30.95$	546	Al

hyperboloid for the crater shape embedded in the known sphere of the initial Dimorphos shape. From this, we can extract the depth as well as the crater diameters (based on the intersection of the hyperboloid with the original surface). We should emphasize that we are examining the transient crater geometries in the results presented in this work, i.e., the initial crater volume following the shock-driven excavation of the crater. To get the true final crater geometry, which will be dictated by the slower motion of the asteroid material flowing in a granular regime, due to the immediate post-excavation motion (typically on the order of a few cm/sec or less) and the low surface gravity of the asteroid, would require models run to much later times than is feasible in these sort of shock-physics hydrodynamic models. To be clear, the limitation here is computational expense: these shock-hydrodynamic models are time-step-limited by the sound speed (which is on the order of a few km s^{-1} in these media), and while in theory we could follow the crater evolution to its final relaxed configuration, in practice this is unnecessary and would require an exorbitant amount of computer time. Once the shock-dominated evolution is completed, the slow friction-dominated granular flow phase can be more efficiently handled by other methods, such as discrete elements or incompressible hydrodynamics, which are not constrained by the very short timescales appropriate for shock-hydrodynamics. Such a follow-on study is outside the scope of this work however, as we are primarily interested in the immediate post-impact ejecta excavation, which dominates the momentum transferred to the asteroid and thereby the resulting deflection.

2.2. CTH Simulations

CTH (Crawford 1999; McGlaun et al. 1990; Hertel et al. 1993) is a large deformation, strong shock wave physics code developed by Sandia National Laboratories. In contrast to the mesh-free ASPH formalism employed by Spheral, CTH uses an AMR (adaptive mesh refinement) Eulerian meshed technique, which provides this study with algorithmic diversity for comparison in our results. The AMR capability is used to refine the simulations around the projectiles and the shock-waves emanating from the impact as the simulations proceed. We apply CTH to model a selection of the scenarios depicted in Figure 2: namely, the uniform Al sphere, DART CAD model (0° orientation), the cylinder configurations ($D = 50$ cm, 100 cm, 150 cm), and the 90° three-sphere model, for a total of six geometries (see Table 3). The uniform Al sphere and DART model are performed in 3D (x, y, z). Because the other

four geometries (the cylinders and 90° three-sphere) are rotationally symmetric about the z-axis, we model these cases in 2D cylindrical (r, z) coordinates. The total volume simulated in CTH varies by scenario: for the DART spacecraft case, the entirety of Dimorphos is represented as is done in Spheral. For the 3D sphere calculation, a smaller box (14 m × 14 m × 14 m) is modeled (centered on the impact point), while the 2D cylindrical coordinate calculations model an 18 m × 18 m box. Outside these boundaries, we use outflow/vacuum boundary conditions. We use as close to the nominal spacecraft mass of 535 kg as possible, but constraints with problem generation result in some deviations from the desired mass: the sphere and three-sphere configurations are closer to 545 kg initial projectile mass—see Table 3 for the exact numbers.

For the materials, we use native CTH material models: SESAME (Johnson 1994; Johnson & Cook 1983) equations of state and strength models appropriate for metals and rock (see Section A.2). Dimorphos is modeled as 30% porous basalt (with the same solid and bulk densities used for pure SiO$_2$ in Spheral), using the SESAME equations of state and brittle damage with localized thermal softening (BDL; Crawford & Schultz (2013)) strength model coupled to a $P - \alpha$ porosity model (Jutzi et al. 2009). The choice of basalt here rather than pure SiO$_2$ as in Spheral and iSALE is a practical one: the basalt equation of state and material properties are better vetted in our CTH implementation, and because basalt is dominantly SiO$_2$, we find this difference to be negligible. We strive to match the basalt material properties in CTH with that used in the other codes (specifically, the material yield strength), but inevitably with models this sophisticated there are differences. BDL is similar to the strength and damage models used in iSALE, as it is based on the model of Collins et al. (2004), to which it adds crack spacing and shear heating estimates within the cracks that create thermal softening. The simple projectiles (sphere, cylinders, and three spheres) are modeled as uniform aluminum (1100-O Aluminum). In order to get the correct DART spacecraft mass and material properties, the spacecraft body is modeled using the same CAD geometry used to initialize the Spheral DART models. We use various SESAME EOSs (equations of state) for the DART components, including aluminum and titanium alloys (Al 6061, AL 2024, Al 7075, and Ti6Al4V) and Stainless Steel 304 to model the structural components of the spacecraft. The strength models applied are the standard SGL (Steinberg–Guinan–Lund; Steinberg & Lund (1989)) models built into CTH for the various alloys listed above. To capture the fabric-like nature of the Roll Out Solar Array (ROSA) panels, we use the Quartz Phenolic SESAME EOS and model it without strength. The ROSA panel material is removed from the CTH calculation at 200 μs after impact, to remedy numerical instabilities introduced by this thin solar panel material. Note, however, that the structural portions of the solar panels remain for the duration of the simulation. The projectile material parameters for the sphere and the full DART spacecraft are summarized in Table 7.

The CTH simulations are run only for the strong cases, as we found inconsistencies in results using the BDL strength model in the weak regime when compared to iSALE and Spheral. In the benchmarking work by Stickle et al. (2020) where we compare these codes, the choice of strength models was similar to those presented here, but only strong targets were considered. The comparison to weak targets using the BDL strength model has not be performed, and we found too many

Table 4
Impactor Input Parameters from iSALE-2D Simulations (Cppr = cells per Projectile Radius)

Shape	Dimensions	Initial resolution	Mass
Sphere	$r = 36.16$ cm (72 cppr)	5.02 mm/cppr	535 kg
Cylinder (D = 150 cm)	$r = 75$ cm (150 cppr)	5.00 mm/cppr	535 kg
Cylinder (D = 100 cm)	$r = 50$ cm (100 cppr)	5.00 mm/cppr	535 kg
Cylinder (D = 50 cm)	$r = 25$ cm (50 cppr)	5.00 mm/cppr	535 kg

differences when we extended to that regime. In this study, we are focused on differences in the outcome due to impactor geometry, so we have chosen not to include weak limit CTH results here, so as not to confuse the issue with too many material modeling differences.

In the CTH models, ejecta material is defined as any material containing a void fraction of greater than zero and less than one, exhibiting positive upward velocity (positive y-direction in 2D, and positive z-direction in 3D), and existing above the "ejecta plane." We define the ejecta plane to occur at a distance of $+1\%$ of the target thickness above the impact plane (80 cm) in order to avoid classifying material that is uplifted but remains attached to the crater lip as ejecta material. The total ejecta momentum is calculated by summing up the momentum of each ejecta particle in the grid. The velocity used is the velocity component perpendicular to the impact plane (y-velocity for 2D and z-velocity for 3D cases).

The transient crater in the CTH models is calculated using an algorithm that measures the depth and the width of the crater by tracking the cells forming the boundary between the target material and void. The depth is measured from the impact plane to the maximum absolute value of the height location for the boundary cells, and the diameter is measured as the distance between cells along the crater boundary profile that intersect the impact plane.

2.3. iSALE Simulations

We use iSALE-2D to model impacts of the aluminum cylinders and single sphere on weak and strong targets in cylindrical (r,z) coordinates (see Table 4). The projectiles are modeled using the Tillotson equation of state (Tillotson 1962) and the Johnson–Cook strength model for aluminum (Johnson & Cook 1983). The targets are modeled using the ANEOS equation of state for SiO_2 (Melosh 2007), which is coupled to the $\epsilon - \alpha$ porosity model (Wünnemann et al. 2006; Collins et al. 2011), and a pressure-dependent strength model (Collins et al. 2004).

iSALE-2D uses 2D cylindrical coordinates, where the left boundary is the axis of symmetry, about which the mesh is rotated. The computational mesh contains a high-resolution domain of equally spaced cells. Initially, the high-resolution domain is 1200 cppr (horizontal) and 1800 cppr (vertical), where cppr is cells per projectile radius (1 cppr $\approx$0.5 cm) in the iSALE models presented here. As discussed in Raducan et al. (2019), to accurately model DART-like impacts and the cratering ejecta, a high spatial resolution is required in order to record the high-velocity particles. Here, we use the regridding option described in Raducan et al. (2019) in order to maintain the high spatial resolution needed to record the fast ejecta at the beginning of the cratering process, while achieving

a reasonable simulation running times of the entire crater formation. The regridding option allows us to coarsen the simulation domain during the crater formation process. The crater sizes and β values from simulations using regridding have been shown to be within 2% of the results from high-resolution, 80 cppr runs (Raducan et al. 2022).

Extension zones are added to the high-resolution domain in order to minimize the shock wave reflection at the computational boundaries and to efficiently increase the mesh size. The extension zones have a proportionally increasing cell size that follows a geometric progression, with an extension factor which is up to 20 times the cell size in the high-resolution domain. The extension zones are useful to simulate the computational domain farther away from the area of interest (i.e., the impact site), without massively increasing the computational cost. Thus, the modeled computational domain is $\approx$65 m (horizontal)$\times \approx$60 m (vertical), which is comparable to the size of the whole asteroid modeled in the Spheral calculations.

To record the impact ejecta, we follow the same approach as in Raducan et al. (2019): Lagrangian tracer particles are placed across the high-resolution domain and their mass, velocity vector, and launch position are then recorded at a fixed altitude, which here is set to 0.5 m above the pre-impact surface. We record each ejecta tracer particle at the time it crosses this plane. Similar to Raducan et al. (2019), we apply a lower velocity threshold to the ejected particles of 10 cm/s, which in our impact scenarios is the minimum speed required to overcome the cohesive strength of the target, and is larger than the escape velocity of the target. In iSALE-2D, the crater radius, depth, and volume are measured at the pre-impact surface level. The crater depth is the distance between the pre-impact surface ($r = 0$) and the crater floor, as measured close to the symmetry axes ($x = 0$). The crater radius is the distance between the crater cavity wall and the symmetry axis.

The careful reader might note that the altitude which material must rise above the surface to be considered ejecta varies slightly between our codes (50 cm for Spheral and iSALE versus 80 cm for CTH). This difference is due to code differences in how ejecta can be analyzed as well as material modeling distinctions—CTH finds some material in the transient crater lip pushes above 50 cm before pulling back for instance. However, this distinction is minor, and prior studies (Stickle et al. 2017; Raducan et al. 2019) have shown small differences in the ejecta threshold altitude do not significantly affect the liberated ejecta momentum, which is our primary metric.

3. Results

3.1. Ejecta

The major diagnostics from the DART mission relate to the ejecta formed from the impact. The primary goal is measuring the deflection velocity of Dimorphos, which is a function of the (known) spacecraft momentum and the (unknown) momentum of any ejecta produced, which could be anything from negligible to many times the spacecraft momentum, depending on the properties of Dimorphos and the impact site. The ejecta we talk about in this study are necessarily fast ejecta, in that they are moving much faster than the escape velocity in order to rise above our threshold altitude in a second or two. These ejecta account for much of the momentum enhancement in
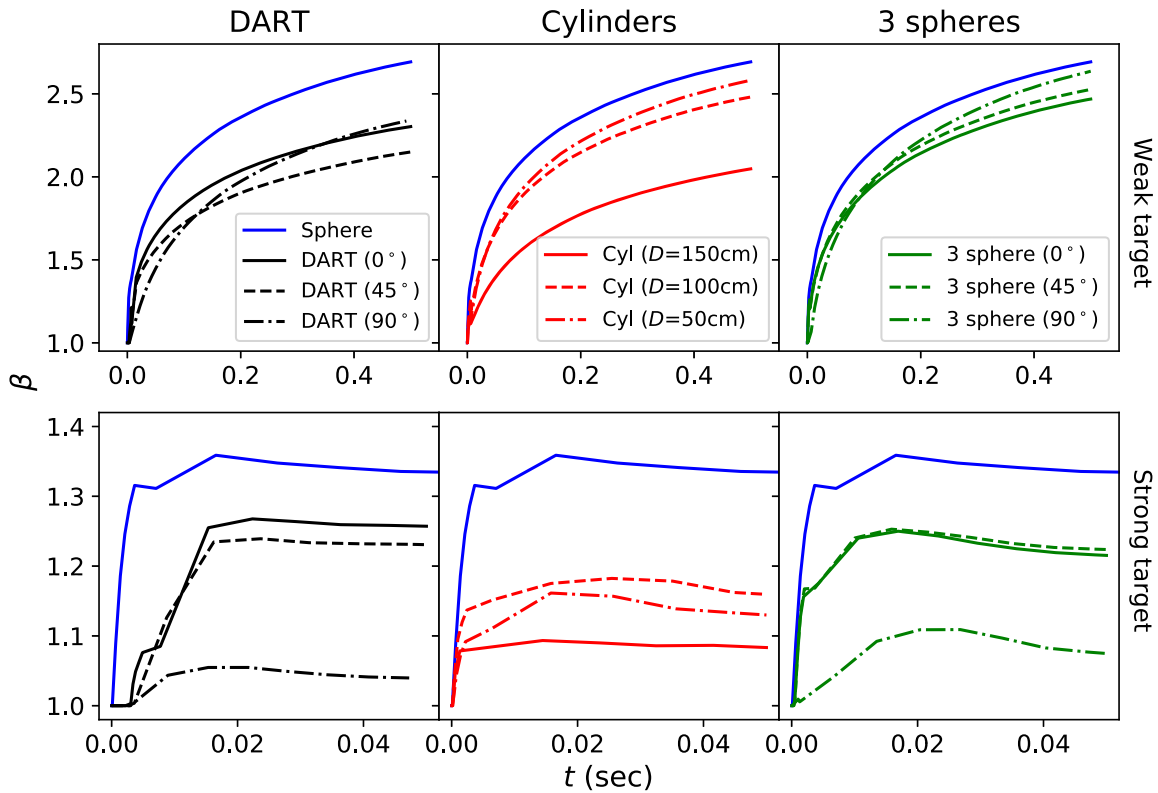
Figure 3. β histories for weak target asteroid material strength (top row) versus strong (bottom row) for our menagerie of models performed in Spheral. The columns are organized by impactor geometry, with DART CAD models in the left column, cylinders in the middle column, and three-sphere geometries in the right column (the sphere result is plotted in each frame for reference). Note that the timescales in the top row are much longer than those in the bottom, because the weak representation of the asteroid produces ejecta over much longer times.

deflecting the asteroid, but there is much more slow moving ejecta material that may barely escape or remain bound to the Didymos/Dimorphos system. That material is outside the scope of our investigation, but other members of the DART investigation team are studying the fate of such slower ejecta, and their results are presented in a separate publication.

The deflection velocity of Dimorphos will be a vector quantity involving the momentum directly imparted by the spacecraft, along with any momentum imparted by the loss of ejecta (via conservation of momentum). Assuming the DART collision itself is inelastic (all the spacecraft momentum is transferred to Dimorphos), the deflection velocity will be

$$\Delta v^{\alpha} = \frac{\Delta p^{\alpha}_{\text{Dimorphos}}}{m_{\text{Dimorphos}}} = \frac{p^{\alpha}_{\text{DART}} - p^{\alpha}_{\text{ejecta}}}{m_{\text{Dimorphos}}}, \quad (1)$$

where $(p^{\alpha}_{\text{Dimorphos}}, p^{\alpha}_{\text{DART}}, p^{\alpha}_{\text{ejecta}})$ are the momenta of Dimorphos, DART, and the ejecta, respectively, and $m_{\text{Dimorphos}}$ the mass of Dimorphos, which we assume is essentially unchanged by the DART event. Note that we are using index notation, so v^{α} is the αth component of the vector $\boldsymbol{v}$.

It is common to parameterize the momentum transfer efficiency from a kinetic impact by β (Rivkin et al. 2021), which is the ratio of the deflection momentum of the target asteroid to the momentum of the spacecraft. In general, this is a complicated expression because the assorted momenta (and resulting deflection velocity) are vector quantities and not necessarily aligned; however, in our case we are impacting a sphere normal to the surface, with the impacting momentum vector aligned along the line connecting the centers of mass of the impactor and target, which reduces this complexity down to

a one-dimensional scalar problem aligned along the z-axis. In this simplified geometry, we can define the β measure of the deflection momentum efficiency as

$$\beta = \frac{\Delta p^{z}_{\text{Dimorphos}}}{p^{z}_{\text{DART}}} = \frac{p^{z}_{\text{DART}} - p^{z}_{\text{ejecta}}}{p^{z}_{\text{DART}}} = 1 + \left| \frac{p^{z}_{\text{ejecta}}}{p^{z}_{\text{DART}}} \right|. \quad (2)$$

We apply the absolute value in Equation 2 to take into account that p^{z}_{DART} is negative (DART is traveling down the z-axis toward Dimorphos, which is centered at the origin), yielding $(p^{z}_{\text{Dimorphos}} < 0, p^{z}_{\text{ejecta}} > 0)$, so in our special alignment, this absolute value simplifies matters. See Rivkin et al. (2021) for a more complete discussion of the definition of β, including the full vector complications.

Figure 3 shows the time evolution of β in the full set of models performed in Spheral. Note that the timescales for the weak (top) and strong (bottom) models to evolve are quite different: the strong Dimorphos models in the bottom row are essentially done by $t = 0.03$ sec, while the weak models are still showing evolution at $t > 0.5$ sec. This difference in timescale with material strength is expected, as both experimental and theoretical studies have shown that cratering processes evolve over longer timescales in weaker material, as do the associated ejecta (Melosh 1989; Holsapple & Housen 2007; Raducan et al. 2022). This long-time evolution makes the weak limit computationally challenging due to the sheer amount of time required to reach the end of the ejecta formation and β evolution. Ideally, we would like to push the Spheral models further, but as a practical limit, the run-time expense of following this many three-dimensional models to
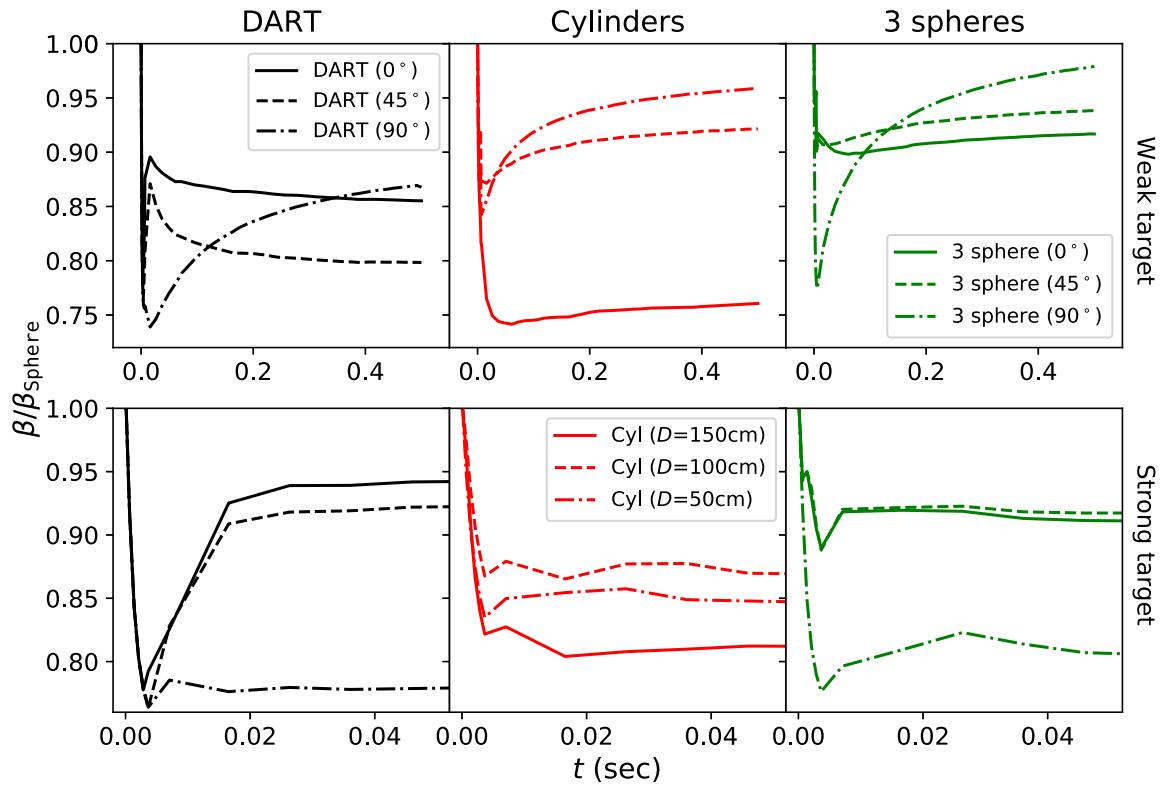
Figure 4. Histories for $\beta/\beta_{\mathrm{Sphere}}$ in the Spheral models. The panels are arranged as in Figure 3.
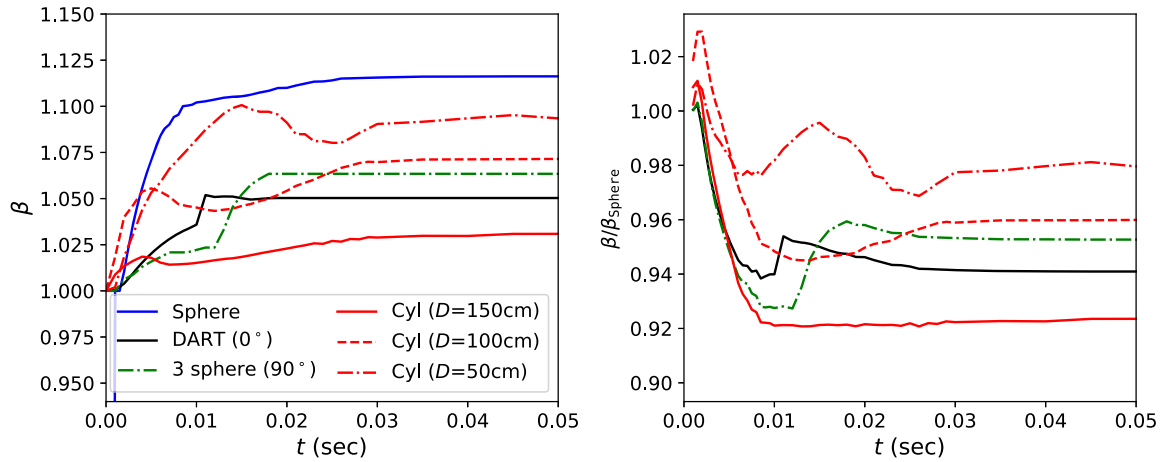

Figure 5. CTH β histories for strong asteroid material strength. The left panel shows the raw β histories for the sphere, DART ($0°$ orientation), and three cylinder configurations, while the right panel shows the ratios with β_{Sphere}.

late times requires us to terminate them when we believe the time evolution of the curves has slowed enough to make the final trends clear.

Since we are primarily interested in how the projectile geometry changes these $\beta(t)$ histories, Figure 4 plots the ratio of $\beta_{\mathrm{proj}}(t)/\beta_{\mathrm{sphere}}(t)$ for each of our projectile geometries (the curves in each panel of Figure 3 divided by the blue curve in that panel). Figures 5 and 6 display the equivalent $\beta(t)$ histories and ratios for CTH and iSALE, respectively. Finally, Figure 7 is an effort to get all the models on the same plot, plotting the final β versus ejecta mass for each scenario across all codes.

Focusing first on the DART CAD model results (left row of Figures 3 and 4, and one result for the $0°$ DART model in Figure 5), we find in all cases that the sphere overestimates the β deflection factor compared with the higher-fidelity DART

representations. Looking at the ratios of $\beta_{\mathrm{DART}}/\beta_{\mathrm{sphere}}$, Spheral finds the sphere overestimates β by 5%–25% in the strong case, while in the weak case it overestimates by 10%–20%. CTH finds a similar degradation of 5% in β for the $0°$ DART scenario in the strong material limit, very close to the Spheral result. It is notable that the relative degradation in $\beta_{\mathrm{DART}}/\beta_{\mathrm{sphere}}$ is much closer between Spheral and CTH than the absolute β values themselves ($\beta_{\mathrm{Spheral}} = 1.25$ versus $\beta_{\mathrm{CTH}} = 1.05$), so this relative reduction in β from projectile geometry appears to be robust with different material model implementations.

There is also an interesting distinction in the effect of DART orientation (see the left column of Figures 3 and 4): for the weak Dimorphos case, the $90°$ DART orientation (i.e., impacting with the solar panels oriented along the direction of travel, end-on) yields the largest β (relative the other
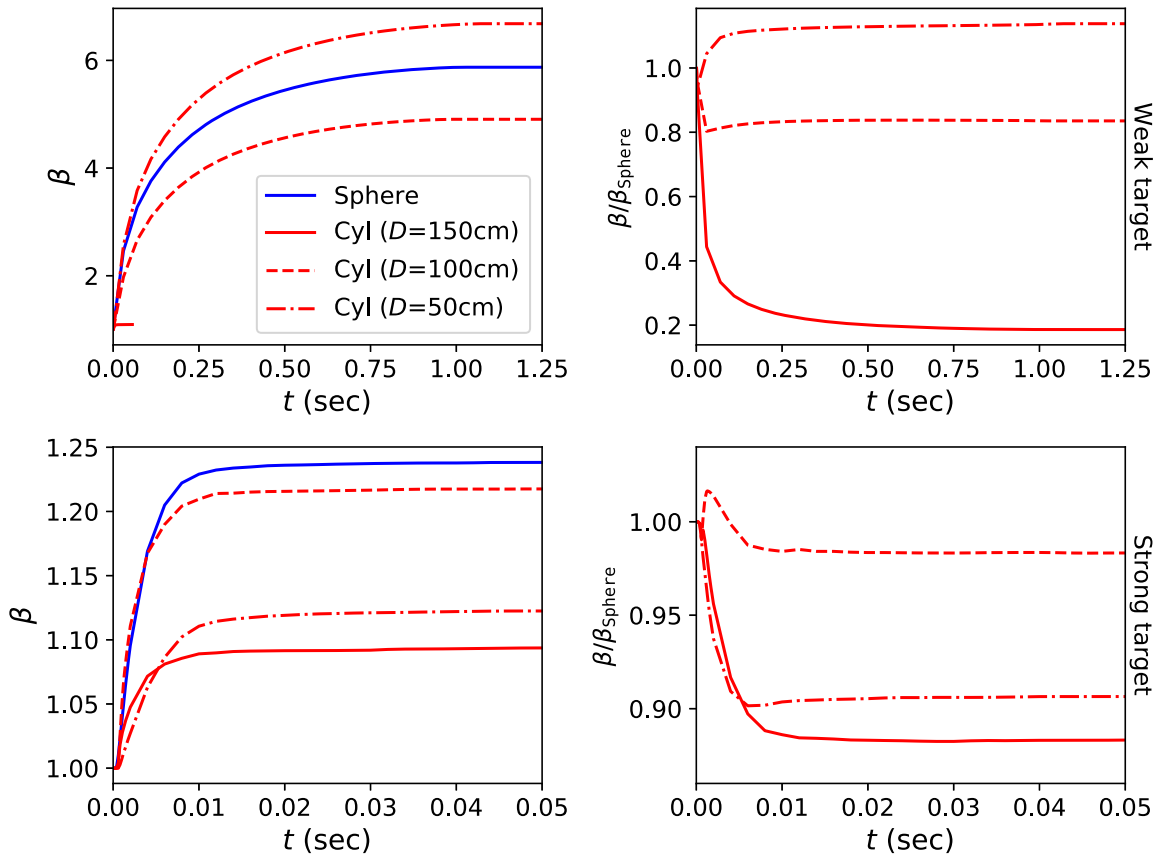
Figure 6. iSALE β histories for strong and weak asteroid material strength regimes. The left panels show the raw β histories for the sphere and three cylinder configurations, while the right panels show the ratios with β_{Sphere}. The top row shows the results for the weak asteroid target, while the bottom row shows the strong Dimorphos case.

orientations, it is still less than the β produced by the sphere), while in the strong material case, this orientation yields the least β by far for any scenario tested. We interpret this as the result of the combination of material strength and porosity. In the strong material case, the large porosity allows the end-on DART configuration to penetrate the most deeply, creating a narrow crater. The would-be ejecta being excavated deep in this crater interact with the strong crater walls of the narrow crater geometry, which slow and can even stop the ejecta, whereas in the weak material case, this deeper material emerges as ejecta and contributes to β. We discuss this point in more detail when we examine the cratering results in Section 3.2.

If this DART orientation dependence of β is a simple impact surface area effect, we would expect to see a similar trend in the cylinder projectile scenarios (middle column of Figures 3 and 4). However, this does not appear to be the case. In the strong limit, the $0°$ DART orientation produces the largest β, while the end-on $90°$ orientation produces the least. This ordering is reversed in the weak material limit, with the $90°$ DART orientation producing the largest β (on a longer timescale). For the cylinders, however, the largest impact area ($D = 150$ cm) always produces the smallest β, while the intermediate and elongated cases ($D=100$ cm, 50 cm) alternate which is the most effective between the strong and weak scenarios; i.e., in the weak limit, the $D=50$ cm cylinder produces a larger β than the $D=100$ cm case, while in the strong limit, this ordering is reversed. There is also a difference in the relative spread of β values: for the DART geometries, we find the strong material limit produces the largest relative spread of β, and in the weak

limit, β is more tightly bunched. The cylinders, however, show a roughly similar spread (percentage-wise) in the strong and weak limits, resulting in a tighter bunching for the strong case and broader range of results in the weak limit, compared with the DART projectile models.

All three codes find a very similar range of β values for the cylinders in the strong material limit: $\beta \in [1.05, 1.2]$, with CTH finding the lowest values, Spheral finding intermediate values, and iSALE finding the largest β. This is most easily seen in Figure 7, where we have plotted the final β versus ejecta mass for all models. In terms of ejecta mass, Spheral finds the largest values (and largest spread between the cylinders), while iSALE and CTH find less ejecta mass in a smaller range. Both Spheral and iSALE find that, in the strong limit, the $D = 100$ cm cylinder (middle value for D) yields the largest β, whereas in the weak material case, $D = 50$ cm (narrowest impactor) is most effective. CTH finds a monotonically increasing relationship of β with decreasing surface area in the strong limit, which is what both Spheral and iSALE find in the weak limit, but not the strong. It appears both iSALE and Spheral indicate there is an optimum elongation for producing β as a function of material strength—CTH may also see a similar effect, but if so, the peak of that relation is not captured in the range of our simple three-value range of diameters.

Looking at the three-sphere impactor geometries (left column of Figures 3 and 4 for Spheral, and one CTH result in Figure 5), we find a number of similarities with the DART impactor results. The $\beta(t)$ time history curves for the $0°$, $45°$, and $90°$ orientations qualitatively match up well for both the

(a) Weak target (Spheral)

(b) Weak target (iSALE)

(c) Strong target (all)
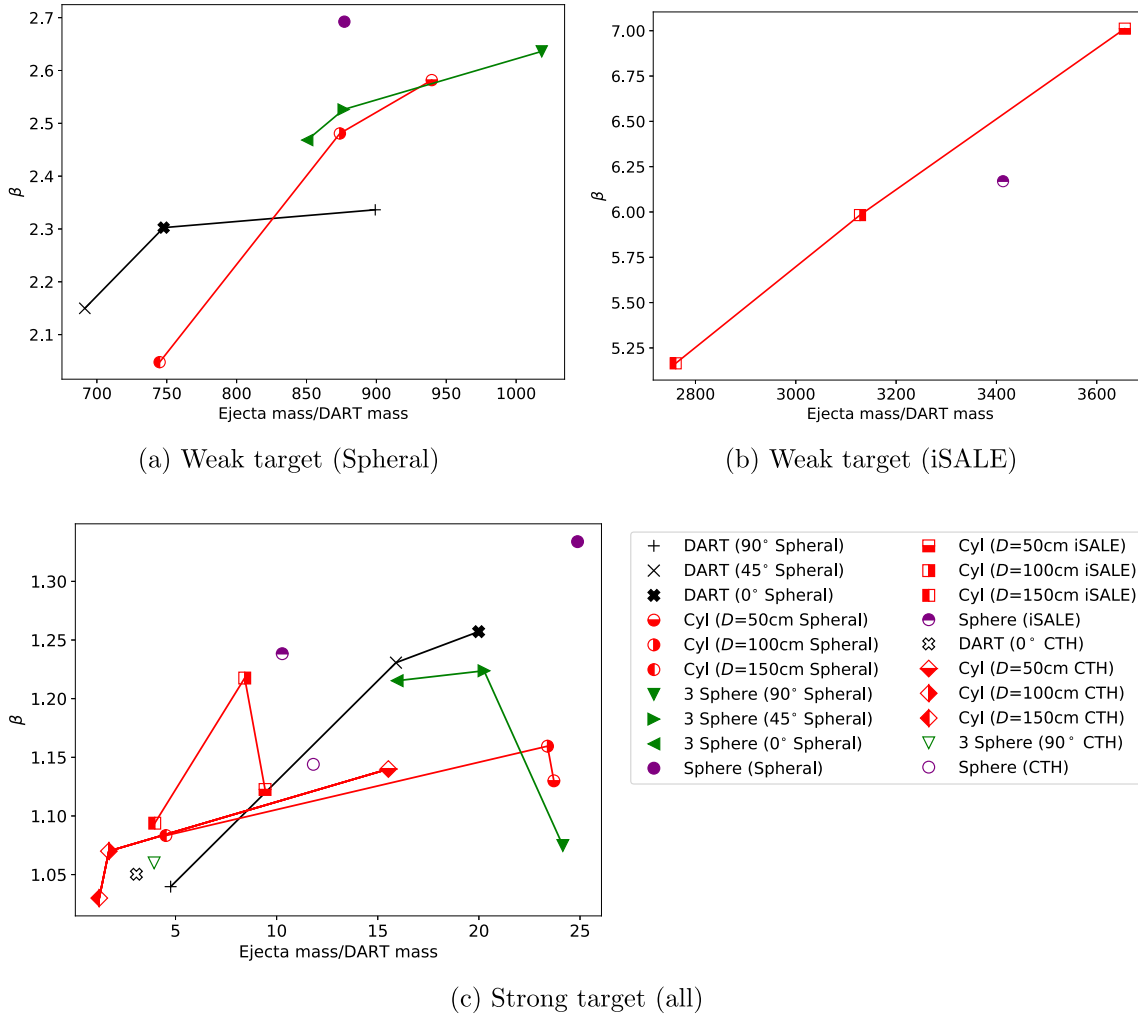
Figure 7. β versus ejecta mass for the various impactor scenarios: weak material results are shown in the top two panels, and strong in the bottom. Note that the range of ejecta mass and β used for the axes of these plots varies between panels.

strong and weak material cases; the trend of how tightly the $\beta(t)$ curves are bunched looks similar, and the ordering of which orientation produces what final β matches for both DART and the three-sphere impactors. In the strong material case, the ratio of reduction in β compared with the spherical impactor is very close to a match comparing the three spheres with the DART model. However, in the weak material case, while the qualitative effect of splitting the impactor into the three spherical components is similar to DART, the raw β values are not reduced quite as much in the three-sphere configuration versus DART. CTH finds less reduction in β for the 90° three-sphere case than does Spheral, which is consistent with the differences between the codes noted in the most elongated cylinders.

Figure 7 plots the produced β as a function of ejecta mass for all our simulations. We have connected the related families of impactors (cylinders to cylinders, DART to DART, etc.) by lines simply to show the associated points. In terms of total ejecta mass produced, it is clear the material strength of the target is far more important than the choice of impactor: while the strong target produces $m_{\mathrm{ejecta}} \sim 10 m_{\mathrm{DART}}$, the weak limit finds $m_{\mathrm{ejecta}} \sim 1000 m_{\mathrm{DART}}$. For a given target strength, we can also see that, while the spherical impactor generally produces the largest β, it does not always yield the largest total m_{ejecta}. In

the weak limit, we can also see that the nonspherical impactors tend to fall along a relationship in $\beta(m_{\mathrm{ejecta}})$, from which the sphere deviates (above in Spheral, below in iSALE). There is also some code variation in measured m_{ejecta}: in the strong limit, Spheral, CTH, and iSALE agree much more closely in β, but vary more significantly in total m_{ejecta}. This is likely a combination of effects. There are certainly material modeling differences that contribute to this difference. For instance, we have gone to some pains to use consistent models for the yield strength of the rocky material (see discussion in Appendices A.1–A.3), but many other physical effects such as the damage model, its parameters, and its effect on other quantities such as the shear modulus are unique to each code. This difference can also be caused by discrepancies in exactly what is labeled as ejecta. The fastest ejecta contributes significantly to β, and is easily identified across codes. However, the slowest material dominates the total ejecta mass, and exactly what low-velocity/altitude cutoff is applied to identify this slow material can exacerbate the total ejecta mass difference even though $\beta(t)$ is less sensitive to this choice. This makes comparing the exact numbers for the ejecta mass more complicated across the codes, as well as highly resolution-dependent, even if they agree fairly well on the ejecta momentum. As the purpose of this study is to identify the
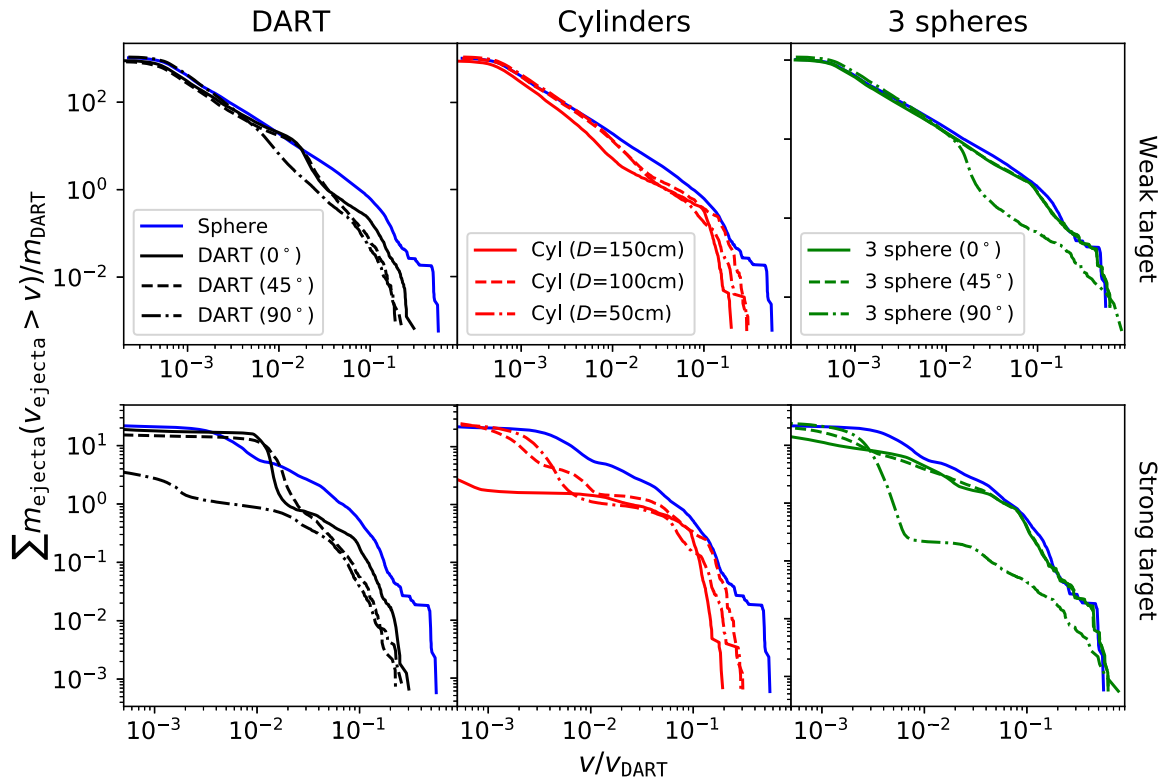
Figure 8. Complementary cumulative ejecta mass functions (of velocity), normalized by DART impactor mass and velocity for the Spheral models.

effect of the projectile geometry (and the primary metric for DART relates to the momentum liberated in ejecta), we have not focused on making the codes as consistent as possible (we refer the reader to the benchmarking study in Stickle et al. (2020) for this purpose). Instead, we have tried to use the best available models and methods for each code, and looked for common qualitative trends with projectile geometry across the models.

Overall, we find a reduction in β when using a realistic spacecraft impactor geometry versus a spherical impactor approximation. It also appears that simply changing the impact surface area (such as we do with the cylinders) does not reproduce the qualitative behavior we see with the true spacecraft geometry, but the multiple impactor analogy of the three-sphere configuration does. Interestingly, although in general we find the nonspherical impactors reduce β compared with the sphere, in the weak limit iSALE finds the most elongated cylinder ($D = 50$ cm) actually produces more β than the sphere. The Spheral results in this case are still growing (albeit more slowly) at 0.5 s after impact when we stop the calculation, so it is quite possible it would also find this elongated cylinder can outperform the sphere in the weak limit, given enough time. It appears the 90° aligned DART impact and 90° three-sphere cases are also still growing in this weak limit, similarly to the $D = 50$ cm cylinder case, and so may also ultimately outperform the sphere given enough time.

In order to better understand where the changes in β are coming from, it is useful to break down the velocity distribution of the ejecta. Figures 8–11 plot the complementary cumulative distribution functions of the ejecta mass and momentum as functions of the ejecta velocity,

$$\overline{F}_{\text{mass}} = m_{\text{DART}}^{-1} \sum m_{\text{ejecta}} (v_{\text{ejecta}}^z > v), \quad (3)$$

$$\overline{F}_p = p_{\text{DART}}^{z}{}^{-1} \sum p_{\text{ejecta}}^z (v_{\text{ejecta}}^z > v). \quad (4)$$

In both the strong and weak limits, we can see the DART impactors produce less high-velocity ejecta than the sphere (Figure 8), which seems to be the bulk of the difference in the final β achieved. The cylinder and three-sphere impactor geometries show a similar reduction in the highest-velocity ejecta compared with the sphere across the codes (see Figures 8 and 9), so this deficit at high velocities appears to be a major factor in reducing the β momentum enhancement versus the sphere. This is consistent with the fact that, while several of the nonspherical impactors actually produce more ejecta mass than the sphere, the final β measurement weights this ejecta mass by its velocity, so this relative loss of high-velocity ejecta becomes more important. Since the highest-velocity ejecta emerge early in the impact and cratering process, this implies that differences due to projectile geometry are created right at the earliest phase of evolution. Another way of viewing the implications of this distinction is that differences in projectile geometry have the strongest effect on the shock wave immediately following the impact, and as the shock propagates farther into the target, these differences begin to fade away. In the strong material case, this early high-speed ejecta is significant in the production of β, but the picture becomes more complicated in the weak material limit, where the sheer amount of material lofted at late times raises the relative importance of the slower ejecta, and we still see some influence of projectile shape on the slowest ejecta. We also find the multiple-impactor three-sphere distributions look more like the DART results than the cylinders, most notably in the strong material $\overline{F}_p$ distributions in Figure 10.
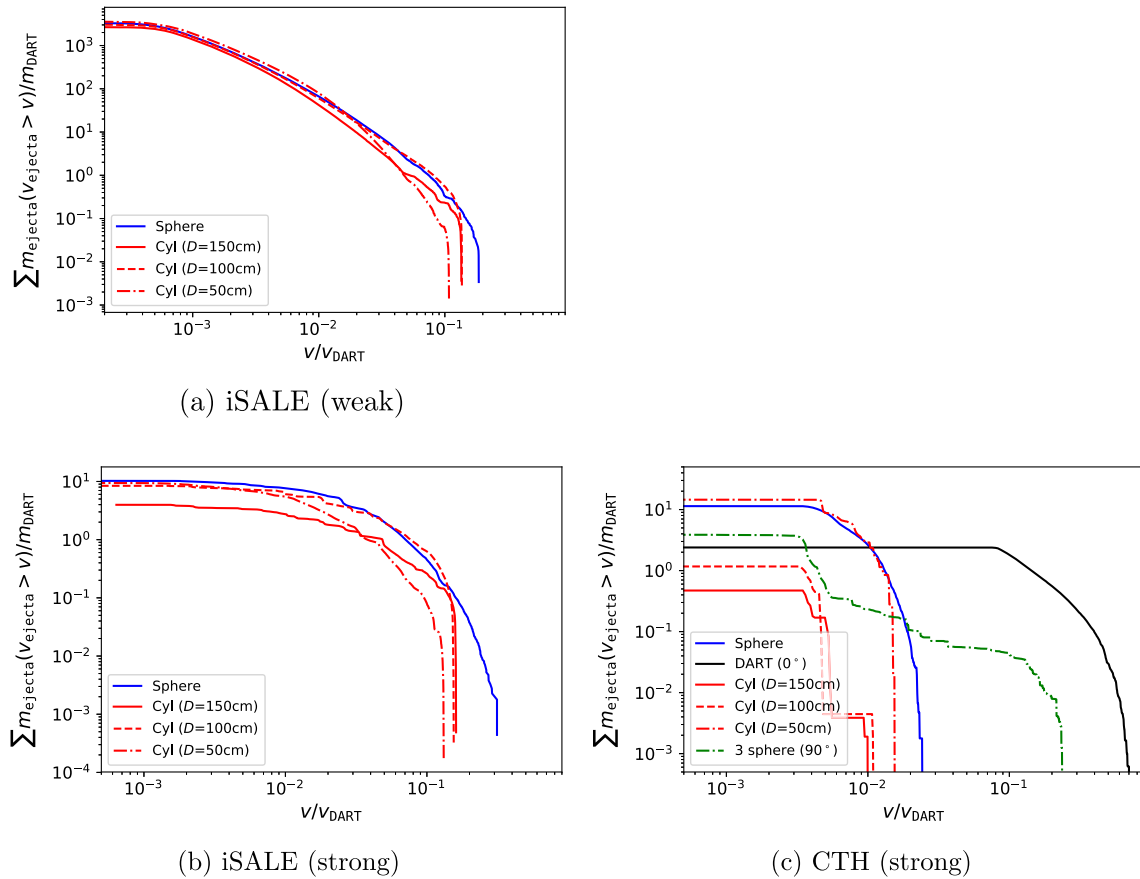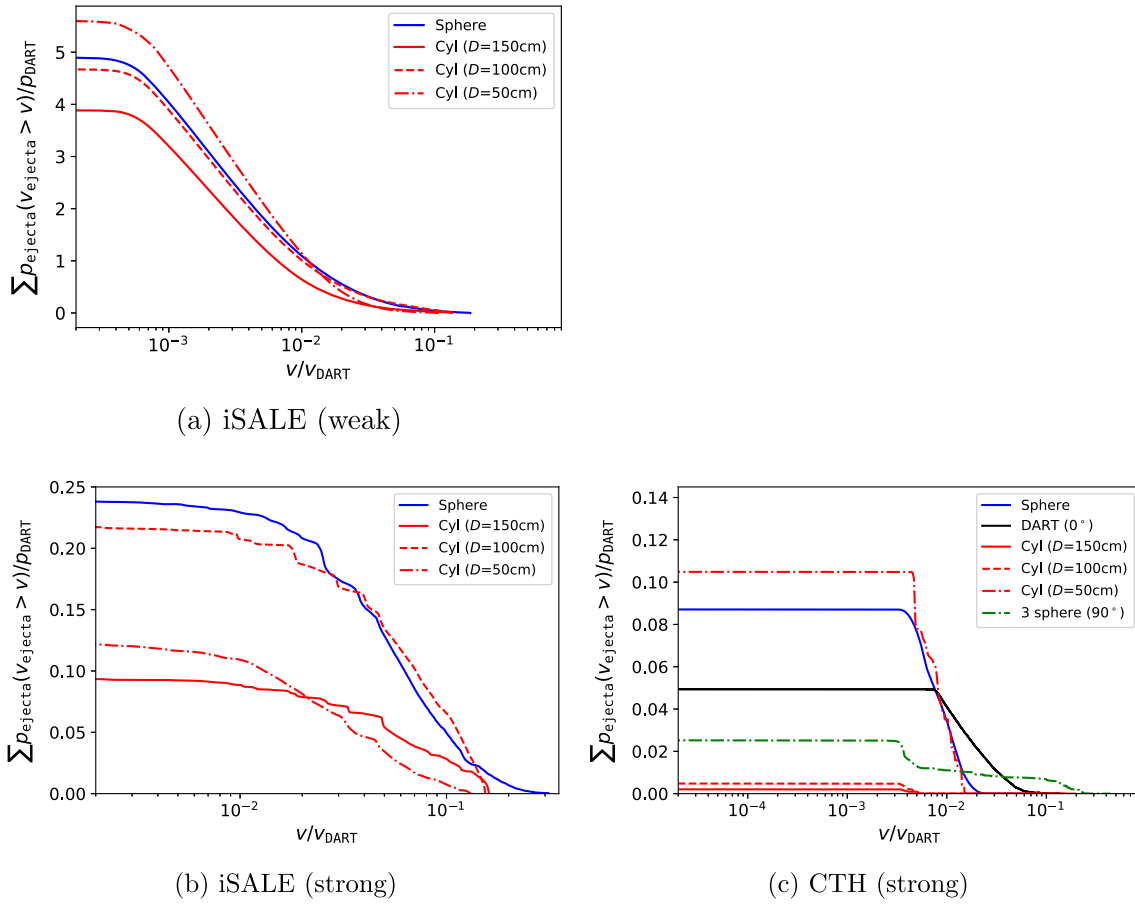
Figure 9. Complementary cumulative ejecta mass functions (same as Figure 8), normalized by DART impactor mass and velocity for the CTH and iSALE models.
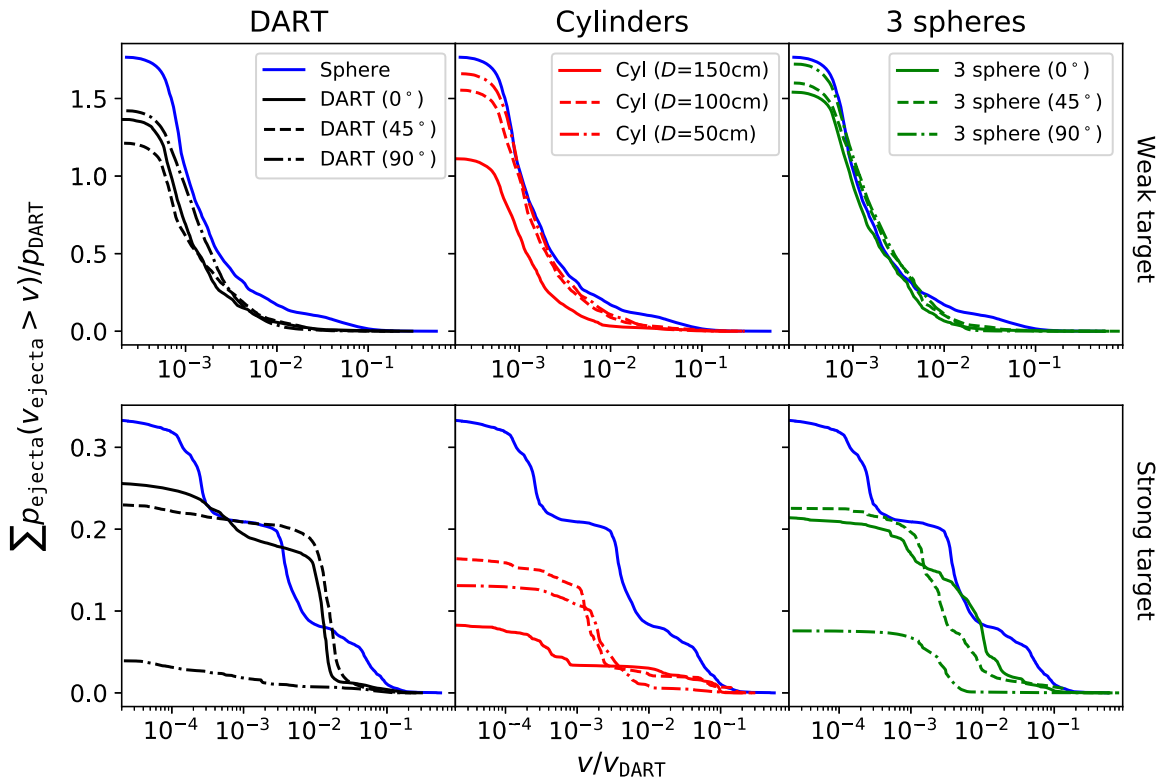
Figure 10. Complementary cumulative ejecta momentum distribution functions (of velocity), normalized by DART impactor momentum and velocity for the Spheral models. Note that the maximum y value on these plots is equivalent to $\beta - 1$.

(a) iSALE (weak)

(b) iSALE (strong)

(c) CTH (strong)

Figure 11. Complementary cumulative ejecta momentum distribution functions (same as Figure 10), normalized by DART impactor momentum and velocity for the CTH and iSALE models.

Comparing the strong and weak material momentum distributions in Figures 10 and 11, we see that a larger fraction of β in the strong limit comes from intermediate-to-fast material, while in the weak limit, β has contributions from all velocity regimes. As described above, this is a consequence of ejecta production continuing for a substantially longer time in the weak limit, while in the strong material limit the transient crater growth is halted at earlier times, terminating the release of material as ejecta that can contribute to β.
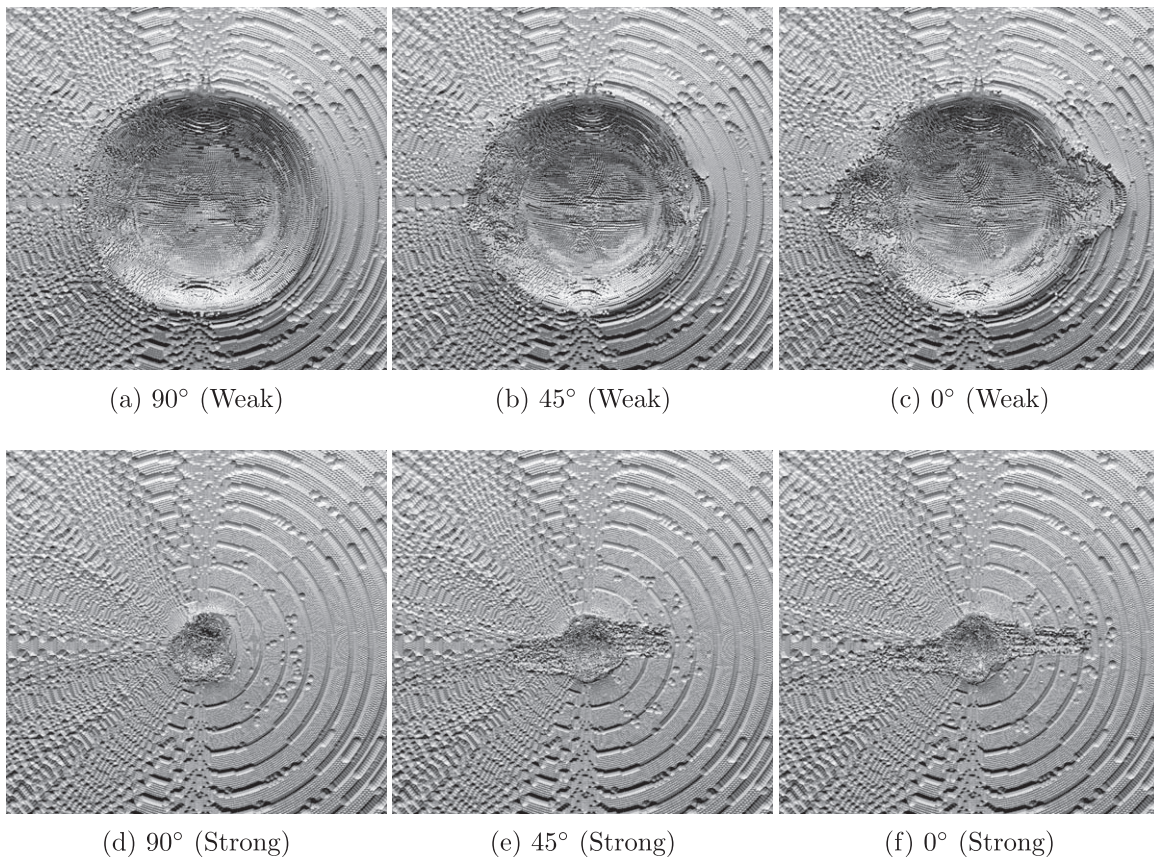
3.2. Cratering

The crater left by the DART impact is also of great interest, though this will not be something either DART nor LICIACube will be able to measure. Fortunately, the Hera mission (Michel et al. 2018) will be able to examine Dimorphos in detail several years after the DART impact. Figure 12 shows renderings of Dimorphos' surface in the Spheral models using the DART impactor in the strong and weak models. Note that these are really the transient crater surfaces, immediately following the shock-driven excavation of the initial crater volumes. Lower-speed evolution of the surface material due to granular flows and the low surface gravity of Dimorphos will evolve these shapes somewhat from this point, likely resulting in wider and shallower volumes.

It is immediately clear that the craters in the weak material (top row) are much larger than those in the strong material (bottom row). The large craters produced in the weak limit

washes out most of the distinction between the impactor used, though we can still see the ends of the elliptical gouges started from the solar array impacts in the weak 0° DART case (the upper right panel of Figure 12). By contrast, in the strong limit, we clearly see the signature of the impactor geometry in the bottom row of Figure 12, right down to seeing how the solar arrays are offset (not in a line) because they are attached to diagonally opposite corners on the DART bus. This sort of detail being captured in the crater imprint is only possible with an initially perfectly smooth surface, such as the one we are modeling here.

Figures 13 and 14 show slices in the y–z plane through the crater volumes in the mass density for all the Spheral models, while Figure 15 shows similar slices through the CTH craters. In the strong limit (Figure 13), Spheral finds the material has been compacted to higher density just below the crater, arresting its development, and the damage has propagated beyond the crater volume, creating lower-density fractures extending much farther into the rock. In the 45° and 90° DART models, we can also see the imprint from the impact of the solar arrays, which create an extended damaged region and some shallow excavation, though clearly the crater volume itself is dominated by the impact of the central bus. There are also some differences in the crater profiles, due to the different orientations: the 90° DART impact leaves a deeper, steeper crater with a more conical shape, versus the more bowl-like shape we see typically. The cylinders show a similar trend with length versus surface area on impact in Spheral, CTH, and

Figure 12. Renderings of the transient crater surfaces for the six Spheral models using the DART CAD impactor geometry (ejecta removed for clarity). The top row shows results for the weak Dimorphos material model, while the lower row is the strong Dimorphos case. The frame size is fixed for each panel, showing a roughly 30 m × 30 m section of the surface. The small-scale crenelations (in ring patterns outside the crater) are artifacts from the polyhedral volume reconstruction around the Spheral ASPH points.

iSALE Figures 13, 15, and 16: the flat disk ($D = 150$ cm) creates the shallowest crater, while the more rod-like configuration ($D = 50$ cm) penetrates more effectively. The three-sphere impactors (only modeled in Spheral and CTH) also show something similar: the spheres impacting in-line (90°) penetrate more effectively, leading to narrower/deeper craters. We believe these morphological differences lead to some effects on the ejecta noted in Section 3.1: the impactors elongated along the direction of impact (90° DART and three-sphere, as well as the $D = 50$ cm cylinder) see some shielding/capture of the ejecta in the crater volume due to interactions with the narrower walls, preventing those cases from efficiently producing ejecta carrying away momentum to contribute to β.
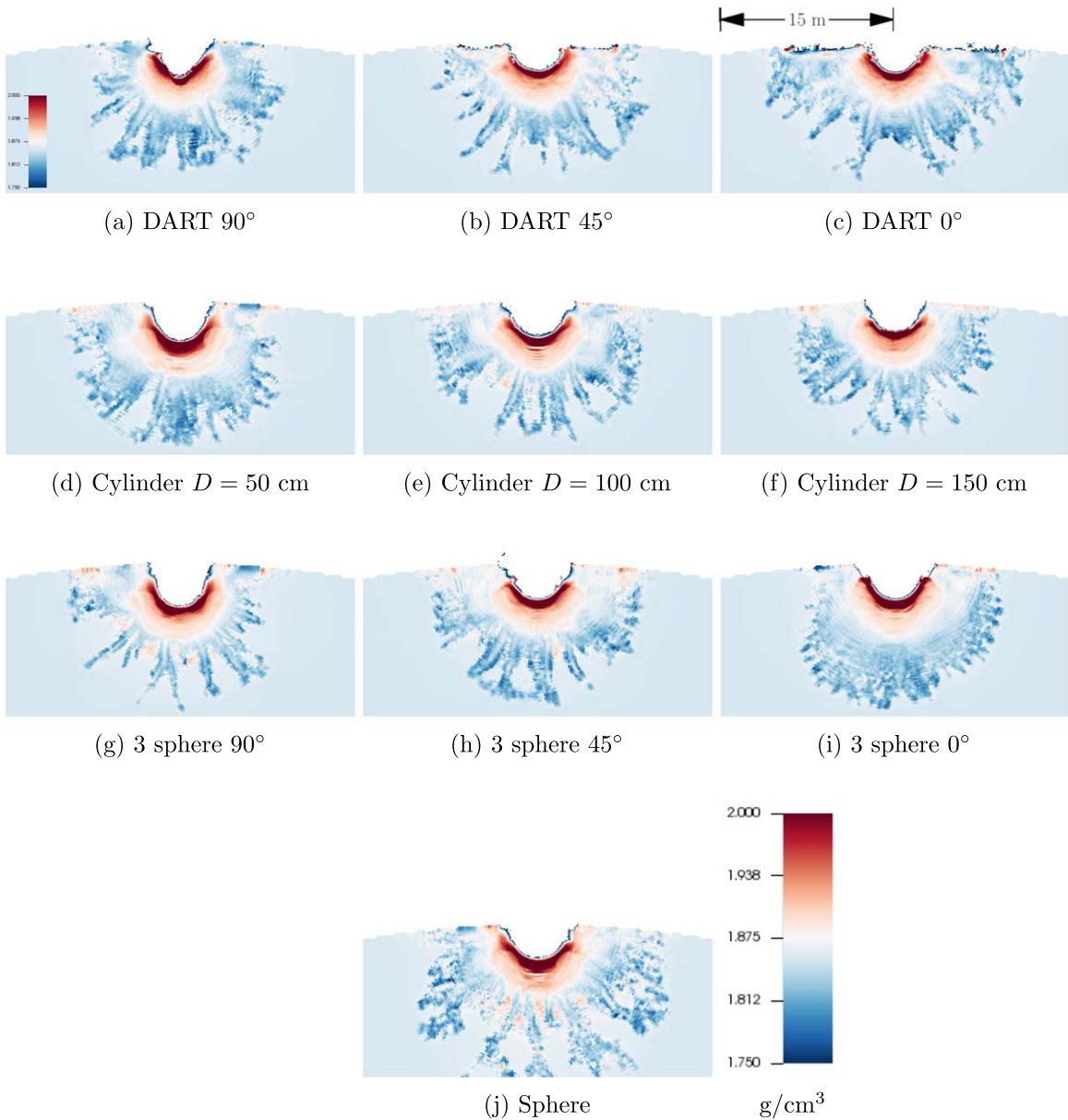
The much larger, shallower crater profiles in the weak material Spheral models shown in Figure 14, however, wipe away most of the distinctions noted in the strong material case above. In this weak limit, we see very similar crater bowls across the variety of impactor types, though there is some remaining signature of the solar arrays in the 0° DART model (upper right panel of Figure 14). We also do not see the same sort of high-density, fractured material below the crater volume we noted in the strong material, case, but rather a smooth transition from low-density immediately at the crater surface to relatively undisturbed material below. This distinct crater wall density profile appears to be due to the fact that outflow from the crater continues for a longer time and excavates a larger volume, so the immediately compressed material from the impact is ejected from the crater rather than remaining in the

crater walls as we saw in the strong limit. As these are transient craters, it remains to be seen if these lower-density crater walls will persist though the final crater formation and relaxation.

In an effort to get more quantitative information about the crater, we extract the transient crater dimensions (width and depth) in our models. The methodology for measuring this geometry varies per code—see discussion in Sections 2.1–2.3 for more details. Figure 17 plots the crater widths versus depth for all our models. Since the Spheral models are 3D, we allow the fit to consider elliptical crater shapes, and the "width" plotted for the Spheral points in Figure 17 is the average of these elliptical diameters—the vertical error bars show the difference between the minimum and maximum axes of the ellipse. The CTH and iSALE points do not have this information, and therefore plot single crater widths per simulation. While all the craters are round to the eye, we can see that the DART models do produce the largest asymmetries in this metric in the Spheral model, though these crater elongations are never greater than 10%. Therefore, while this crater eccentricity is barely discernible in these idealized (i.e., impact onto a perfectly homogeneous surface) cases, and it does distinguish the DART models from the idealized impactors (which produce rounder craters), we do not expect this level of difference to be measurable for real impact conditions on rough, inhomogeneous targets, like Dimorphos is likely to be.

In the strong material case, we see a tight spread in the crater geometry for Spheral (width $\in$ [3.5, 5.5] m, depth $\in$ [1.5, 3] m),

(a) DART 90°   (b) DART 45°   (c) DART 0°

(d) Cylinder $D = 50$ cm   (e) Cylinder $D = 100$ cm   (f) Cylinder $D = 150$ cm

(g) 3 sphere 90°   (h) 3 sphere 45°   (i) 3 sphere 0°

(j) Sphere   g/cm³

Figure 13. y–z slice through the mass density for the Spheral models of the strong Dimorphos case at $t = 0.05$ s after impact, showing the crater profile in this plane. The visualized box is 30 m across the horizontal in these images, and all share the same color bar shown in the upper right (DART 90°) panel, spanning $\rho \in [1.75, 2]$ g/cm⁻³. The inset length-scale bar on the upper right is 15 m. The lower-density fractured material extending into the body of the asteroid below the crater is evident in these images.

with the symmetric impactors like the sphere representing the high end of the range and the DART impactors the low. CTH finds very similar crater width and depth for the DART 0° model. For the spherical impactor, we see a range of results between the codes, with iSALE finding the smallest crater, Spheral finding an intermediate size, and CTH finding the largest crater in terms of width and depth. In general, in the strong limit, Spheral and iSALE are fairly close, while CTH predicts slightly larger craters of width $\in [6, 9.5]$ m and depth $\in [4, 5]$ m.

In the weak limit, we see more of a spread between Spheral and iSALE: Spheral finds (width, depth) $\sim (29, 10)$ m, while iSALE finds (width, depth) $\sim (21, 7.5)$ m. Both codes find the crater geometry between the different projectile types is tightly clustered around these averages, so they agree that, in the weak

material limit, the resulting crater geometry is only weakly dependent on the projectile geometry.

Overall, we find there is some influence of impactor type on the resulting crater dimensions. However, it is clear that sensitivity to the material parameters far outweighs any variation we see here from our impactor geometry suite. Based on these results, the unconstrained parameter space for the asteroid material properties and its surface structure will likely play a larger role in influencing the crater morphology compared to the geometry of the impactor.

4. Conclusions

In this study, we examine the effect of a realistically shaped impactor on the outcome of kinetic impactor missions such as DART, focusing on how the projectile geometry affects the
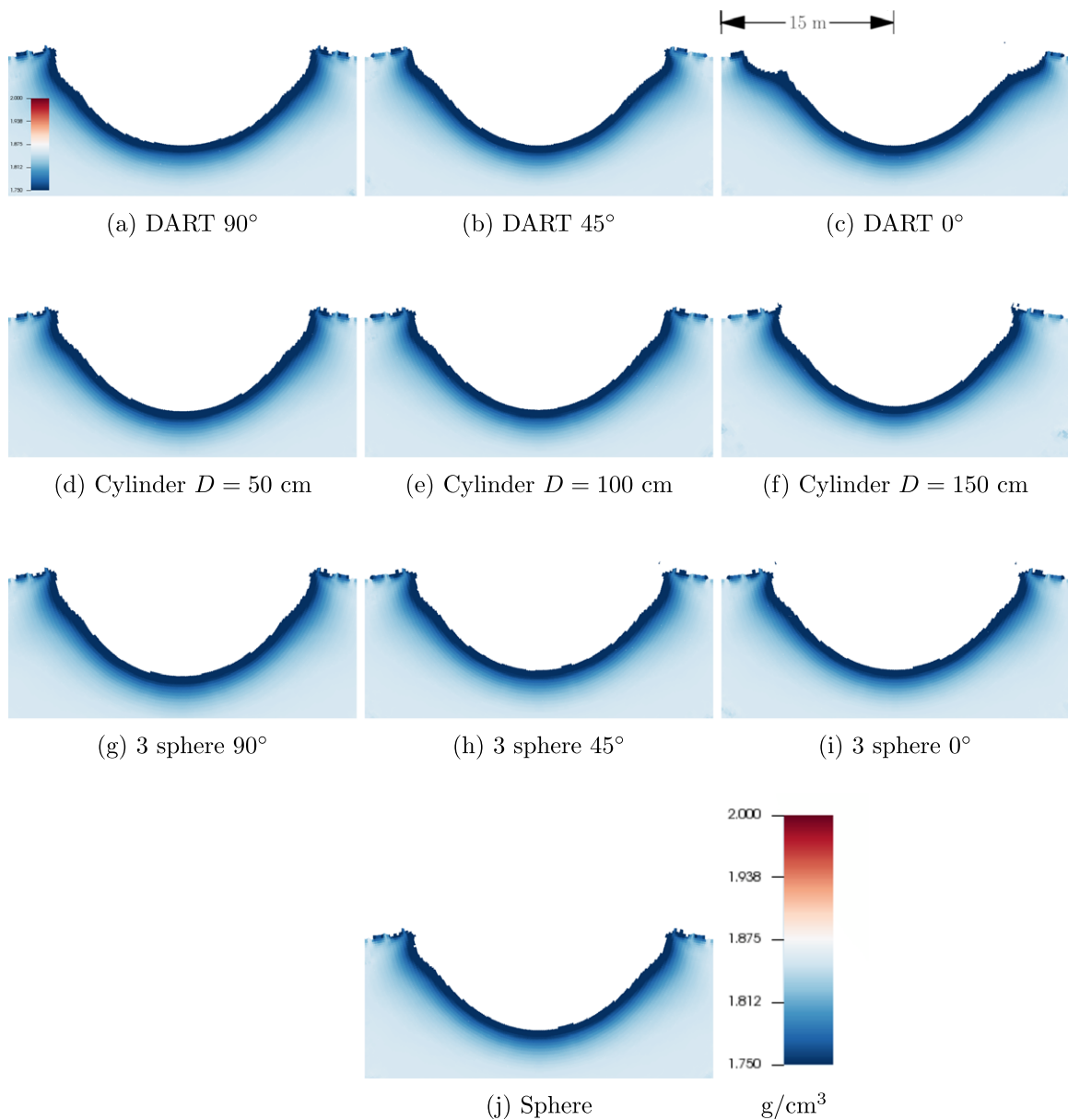
Figure 14. Same as Figure 13 for the Spheral models of the weak material limit at $t = 0.5$ sec after impact. Note that these slices are on the same scale as those in Figure 13 (30 m across each slice box, with the color bar spanning $\rho \in [1.75, 2]$ g/cm^{-3}), demonstrating how much wider the craters are in this material strength regime. Note also that the compressed and fractured material is largely excavated as well, compared with the strong limit.

resulting ejecta momentum and cratering compared with the results when using idealized impactor geometries (such as a sphere) with the same mass and impact momentum, which are commonly assumed to be a sufficient representation of the impactor in numerical models and laboratory experiments. We find that, in the limit of strong asteroid target material, assuming an idealized impactor such as a solid sphere can overestimate the ejecta momentum enhancement β (Equation (2)) by 5%–25%, while for weak material this overestimate is on the order of 10%–20% (depending on spacecraft orientation). Much of this difference is due to differences in the fast ejecta, which emerge early in the cratering process and therefore are most influenced by the details of the impactor. While the effect of projectile geometry is less significant than other unknowns about the asteroid itself (material strength properties, impact angle, and terrain

or the presence of boulders can affect ejecta momentum by factors of $\gtrsim 2\times$), it is non-negligible, particularly in an experiment such as DART where determining the β ejecta momentum enhancement factor is a primary requirement. We consider various idealizations of the impactor to see how well they can reproduce the effect of the true spacecraft geometry, and we find that creating a simplified multiple impactor scenario (our so-called "three-sphere" approximation) is fairly successful at reproducing the qualitative (and approximate quantitative) effects. We also find that simply changing the impact surface area in a single impactor (the assorted cylinder geometries considered here) does not match the qualitative spacecraft results well. This suggests the spacecraft behaves more like a multiple impactor than a distorted single impactor, at least in regard to the diagnostics related to the ejecta we are primarily concerned with. Alternatively, we can simply
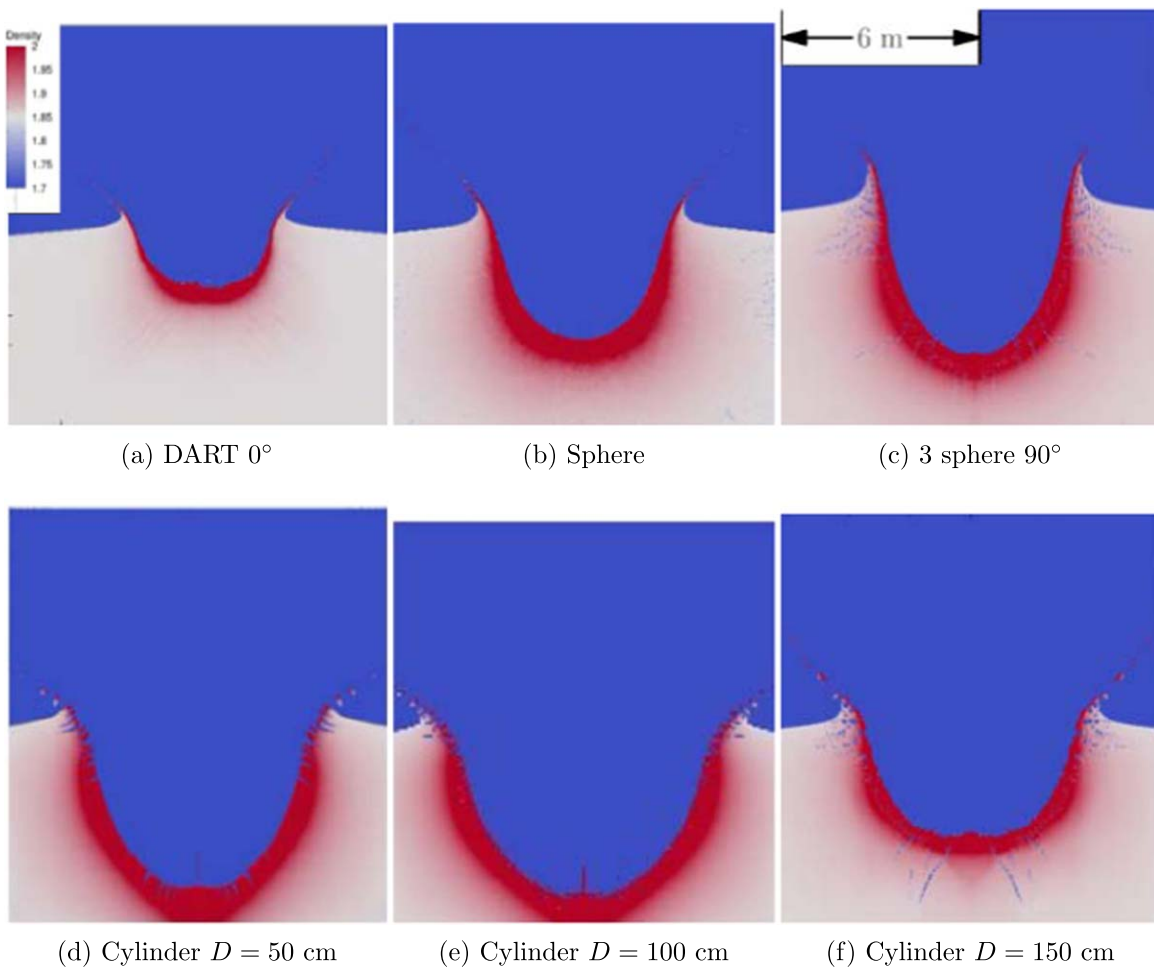
Figure 15. Mass density slices through the CTH craters in the strong Dimorphos models. All frames are at $t = 0.03$ s after impact, except the DART 0° panel, which is shown at $t = 0.019$ sec. Each panel is 12 m across, so these are zoomed-in relative the Spheral results in Figures 13 and 14. Note that the blue region in these figures is vacuum.
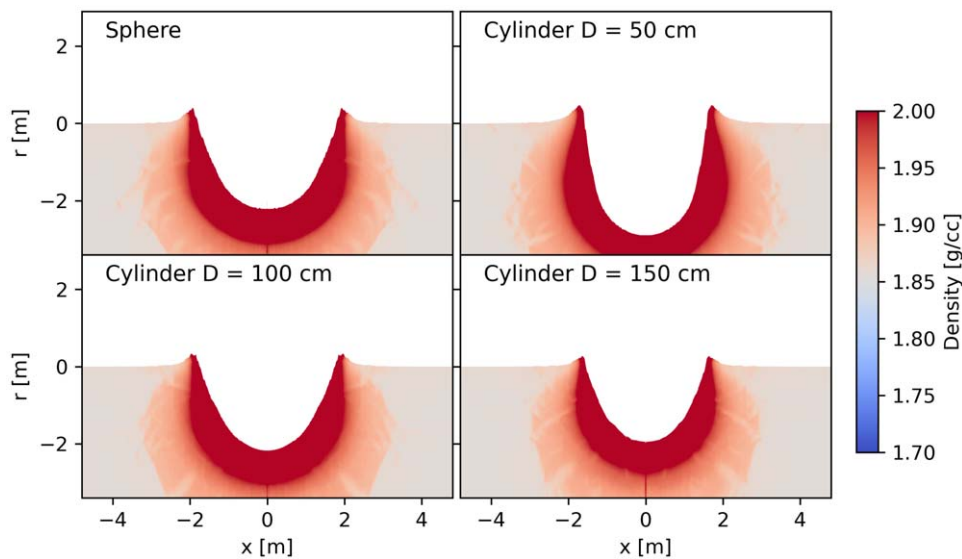
Figure 16. Transient crater profiles from the iSALE-2D simulations of the strong Dimorphos scenarios. All frames are at $t = 0.05$ s after impact.

recognize that an idealization such as the spherical impactor represents a limiting case, and the full spacecraft reality will likely be somewhat reduced compared with this idealization. Table 5 summarizes the calculated deflection velocity

(Δv, calculated from Equation (1) and our final β values) for all of the impactor scenarios presented in this paper, to demonstrate the sensitivity of a primary DART measurable diagnostic to this impactor geometry variation and give a

(a) Weak (Spheral)

(b) Weak (iSALE)

(c) Strong (all)
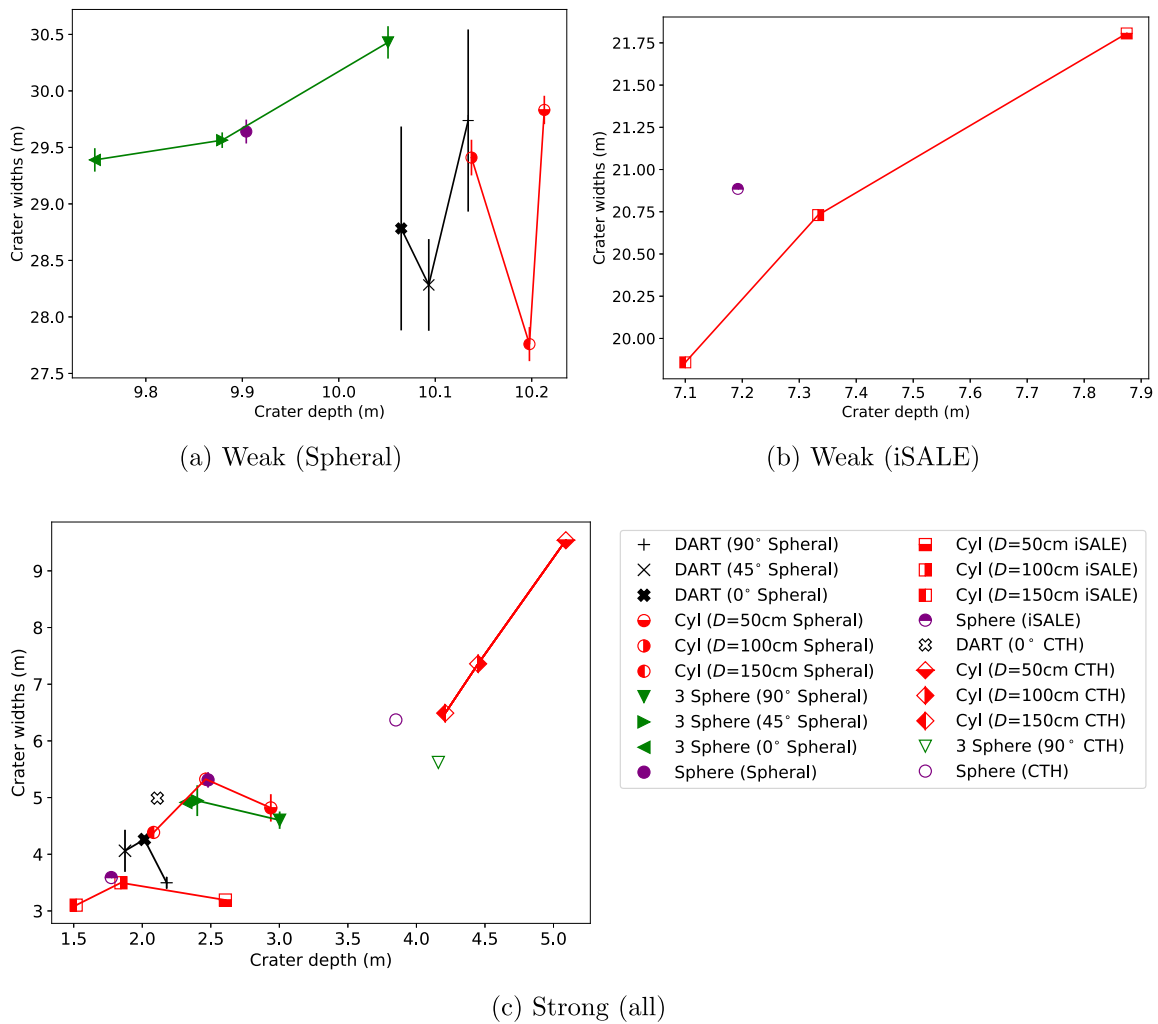
Figure 17. Crater width versus depth for the strong (bottom) and weak (top) Dimorphos material models. The error bars on the width axis (for the Spheral result—the other codes run in 2D $r-z$ geometry do not have this information) show the spread of the minimum and maximum semimajor axes of the ellipse representing the intersection of the hyperboloid and the original Dimorphos surface. Note that the range varies between panels in the weak material results, in order to zoom in on the points in each case.

Table 5
Deflection Velocities (mm s^{-1})

Impactor	Spheral		iSALE		CTH
	Strong	Weak	Strong	Weak	Strong
Sphere	1.19	2.41	1.11	5.52	0.998
DART (0°)	1.12	2.06	⋯	⋯	0.939
DART (45°)	1.10	1.92	⋯	⋯	⋯
DART (90°)	0.930	2.09	⋯	⋯	⋯
Cylinder $D = 150$ cm	0.969	1.83	0.978	4.62	0.924
Cylinder $D = 100$ cm	1.04	2.22	1.09	5.35	0.898
Cylinder $D = 50$ cm	1.01	2.31	1.00	6.27	0.913
Three-sphere (0°)	1.09	2.21	⋯	⋯	⋯
Three-sphere (45°)	1.10	2.26	⋯	⋯	⋯
Three-sphere (90°)	0.961	2.36	⋯	⋯	0.951

sense of how these β momentum enhancements translate to the actual deflection velocity.

In terms of the transient (immediately post-impact) crater geometry, we find much less sensitivity to the impactor structure, especially in the weak asteroid material case. It is therefore unlikely that the spacecraft geometry approximations in modeling will affect the metrics we can measure after the experiment, such as those obtained by the Hera mission, which will characterize the Didymos system and post-DART Dimorphos state, including the DART crater.

We also find that the asteroid material strength plays a role in how the projectile geometry affects the impactor observables (ejecta and crater), both in quantitative measures as well as the trends with shape. For strong target material, we find that impactors elongated along the direction of impact (such as turning the spacecraft to align the long axis with the direction of impact) causes the ejecta momentum and β to be reduced, while the opposite is true for weak target materials. This effect is captured well by the three-sphere impactor surrogate, but less so by simply taking a uniform rod and stretching or compressing it in the direction of travel. We also find that the resulting crater geometry is more influenced (though still not a large effect) by the impactor geometry for strong target materials, while the difference is almost entirely washed away in the weak material limit.

In this paper, we deliberately chose to model a wide range of material strengths in order to explore how this might change the sensitivity to projectile geometry, but where the actual material

properties of Dimorphos fall in this spectrum is unknown. Our strong material limit is chosen to mimic fully competent rocky material such as solid rock we might encounter on Earth, while the weak limit is chosen to look more like loosely cohesive regolith-like material. It seems likely, based on observations during the surface sampling in the OSIRIS-REx mission (Lauretta et al. 2017), as well as the SCI (Small Carry-on Impactor) experiment carried out at Ryugu by the Hayabusa2 mission (Arakawa et al. 2020), that the weak material limit is the most likely case. In fact, if Dimorphos' surface is as weak as that observed during the SCI experiment (where the impactor was seen to produce ejecta for minutes after the impact and the resulting crater was estimated >10 m in diameter; Arakawa et al. (2020)), it could be significantly weaker than even the weak limit presented here. If so, based on this and prior studies, we can expect to see larger β values and larger craters for weaker materials, so we will certainly learn a great deal about the material properties of Dimorphos from the outcome of the DART impact.

Appendix
Material Models

A.1. Spheral

In Spheral, we use an ANEOS quartz equation of state for the asteroid material (Thompson & Lauson 1972; Melosh 2007; Thompson et al. 2019), while the various impactor materials (Al, Ti-6Al-4V alloy, stainless steel, and Si; see Table 1) are modeled using the LEOS (Livermore Equation of State) library (Fritsch 2016). The porosity of the asteroid material is modeled using a strain-alpha ($\varepsilon - \alpha$) prescription as described in Wünnemann et al. (2006); Collins et al. (2011) (parameters summarized in Table 6).

Damage is evolved per ASPH point, and is based on a stochastic model assuming the distribution of initial flaw strains

Table 6
Material Parameters Used in Spheral for Asteroid Rock

	Strong	Weak
Material	SiO$_2$	
Equation of state	ANEOS	
ρ_0, reference (solid) density	2.65 g cm^{-3}	
$P_{\min}$, minimum pressure (solid)	-100 MPa	
$P_{d_{\min}}$, minimum pressure (damaged)	0 MPa	
Strength model		
Y_{s0}, yield strength at $P = 0$ (solid)	100 MPa	0.1 MPa
Y_{d0}, yield strength at $P = 0$ (damaged)	10 MPa	0.01 MPa
$Y_{s\infty}$, yield strength at $P = \infty$ (solid)	3.5 GPa	
$Y_{d\infty}$, yield strength at $P = \infty$ (damaged)	1.5 GPa	
f_s, coefficient of friction (solid)	1.2	
f_d, coefficient of friction (damaged)	0.6	
G_s, shear modulus (solid)	22.7 GPa	
G_d, shear modulus (damaged)	227 MPa	
Porosity model		
ϕ_0, initial porosity	0.3	
ρ_{bulk}, initial bulk density	1.855 g cm^{-3}	
ϵ_E, elastic compaction limit	-1.88×10^{-4}	
α_X, distension at power-law transition	1.0	
κ, exponential factor for distension	0.9	
Damage model		
k, Weibull power-law constant	5×10^{24} cm^{-3}	
n, Weibull power-law exponent	9.0	

is distributed according to a Weibull distribution,

$$n_f(\varepsilon_f \leqslant \varepsilon) = k\varepsilon^m, \tag{A1}$$

where $n_f(\varepsilon_f \leqslant \varepsilon)$ is the number density of flaws with activation strains $\varepsilon_f < \varepsilon$, and (k, m) are material dependent constants. This is the same material assumption used in the standard Benz & Asphaug damage model (Benz & Asphaug 1994, 1995) commonly employed in SPH models for failure of rocky materials. For the asteroid material, we use (k,m) values appropriate for basalt (see Table 6). The full Spheral damage model is a tensor extension of the Benz & Asphaug algorithm (defining a tensor damage value per point i: $D_i^{\alpha\beta}$), appropriate for materials with varying resolution. A full description of this model is beyond the scope of this paper and will appear in a future publication, though some background is available in Owen (2010). We also note that damage is applied for the impactor materials as well, but the exact parameters used are not important, as the impactor components are entirely damaged once impact occurs, with strains well beyond any reasonable failure criteria.

The relevant strength model for the asteroid material in Spheral consists of how we treat the yield strength (Y) and shear modulus (G) in the presence of damage. We reduce the full tensor damage $D_i^{\alpha\beta}$ to a scalar value D_i for the purposes of damaging these strength values by taking the maximum eigenvalue of the damage,

$$D_i \equiv \max[\text{Eigenvalue}(D_i^{\alpha\beta})]. \tag{A2}$$

The yield strength is treated in the same manner as the ROCK model in iSALE, which is slightly generalized from the original description in Collins et al. (2004). The yield for each point varies as a function on the local point-wise damage

variable D_i linearly between a solid yield strength Y_s and damaged yield strength Y_d:

$$Y = (1 - D)Y_s + DY_d. \tag{A3}$$

In this and the following equations, we drop the i subscript and implicitly note these relations are defined per ASPH node, so $D \equiv D_i$, $Y \equiv Y_i$, etc. The solid (or intact) rock strength is defined by smooth approximation to experimental data first defined by Lundborg (1967),

$$Y_s = Y_{s0} + \frac{f_s P}{1 + f_s P/(Y_{s\infty} - Y_{s0})}, \tag{A4}$$

and the damaged yield strength is given by a Drucker–Prager relationship,

$$Y_d = \min(Y_{d\infty}, Y_{d0} + f_d P). \tag{A5}$$

In these equations, P is the pressure, $(Y_{s0}, Y_{s\infty})$ the intact (solid) yield strength at zero and infinite pressure, $(Y_{d0}, Y_{d\infty})$ the damaged yield strength at zero and infinite pressure, and (f_s, f_d) the coefficient of friction for solid and damaged material. The values used for these parameters are given in Table 6. For further discussion on this yield strength model for rock, see Collins et al. (2004), Raducan et al. (2019), and Lundborg (1967).

The shear modulus for rock varies linearly between the solid (undamaged) limit G_s and damaged value G_d

$$G = (1 - D)G_s + DG_d. \tag{A6}$$

Spheral also allows the specification of minimum pressures $P_{\min}$ (undamaged) and $P_{d_{\min}}$ (damaged), which are applied in a similar fashion

$$P = \max[(1 - D)P_{\min} + DP_{d_{\min}}, P_{\text{EOS}}], \tag{A7}$$

where P_{EOS} is the pressure returned by the equation of state.

A.2. CTH

The CTH models use CTH's native equations of state and strength models. The simplified projectiles (spheres and cylinders) are modeled as aluminum, using the Los Alamos National Lab (LANL) SESAME equation of state (Johnson 1994). The SESAME EOS is a database of tables that relates pressure and internal energy to temperature for a variety of materials. This EOS is derived from both experimental and theoretical data, making it extremely accurate, and it has been widely used in impact simulations (Campbell 1998; Heberling et al. 2018). For the material strength models, we use the Steinberg–Guinan–Lund (SGL) strain-rate constitutive model for 1100-O Aluminum, which is defined as a standard option within CTH (Steinberg & Lund 1989; Taylor 1992).

The target material is modeled as 30% porous basalt using the SESAME equation of state (Barnes & Lyon 1988), and employs the $P - \alpha$ porosity model, which considers part of the incident kinetic energy delivered by the impact to dissipate by pore compaction (Jutzi et al. 2009). In order to model the geologic basalt material in the target in the strong limit, we use the Brittle Damage with Localized Thermal Softening (BDL) strength and damage model (Crawford & Schultz 2013; Schultz & Crawford 2016; Crawford 2020), which describes both the strength and failure/fracture of the target material—see Table 7 for material parameters. In brief, BDL is a pressure-dependent yield and brittle damage model that is based on the popular

Table 7
CTH Material Model Parameters

Description	Projectile	Target
Material	Al	Basalt
Equation of state	SESAME[a]	SESAME[b]
Strength model	SGL[c]	BDL[d]
ρ_0, reference density	2.707 g cm^{-3}	2.65 g cm^{-3}
ν, Poisson ratio	0.330	0.250
Strength/Damage model		
Y_{s0}, yield strength at $P = 0$ (solid)	⋯	90 MPa
Y_m, von Mises plastic limit	⋯	3.5 GPa
f_s, coefficient of friction (solid)	⋯	1.8
f_d, coefficient of friction (damaged)	⋯	0.8
Brittle-ductile transition pressure	⋯	2.56 GPa
Brittle-plastic transition pressure	⋯	4.11 GPa
Brittle-plastic transition pressure at max failure strain	⋯	8.22 GPa
Tensile strength	⋯	-100 MPa
Y_∞, yield strength at $P = \infty$	⋯	8.22 GPa
Damage at failure	⋯	0.7
T_m, melting temperature	⋯	0.160 0 eV
Porosity model: $P - \alpha$ (pumice)		
ϕ_0, initial porosity	⋯	0.3
α_0, initial distension parameter	⋯	1.44
ρ_{bulk}, initial bulk density	⋯	1.85 g cm^{-3}
Transition from elastic to plastic regime	⋯	1 MPa
Pore compaction pressure	⋯	280 MPa
Y_0, internal yield stress	40 MPa	⋯
Y_M, maximum yield stress	480 MPa	⋯
G_0, internal shear modulus	27.1 GPa	⋯
A, material constant	6.52×10^{-12} Pa^{-1}	⋯
B, material constant	7.15 eV^{-1}	⋯
γ_0, initial Gruneisen coefficient	1.97	⋯
T_m, melting temperature at constant volume	0.105 3 eV	⋯

Notes.
[a] Johnson (1994)
[b] Barnes & Lyon (1988)
[c] Taylor (1992)
[d] BDL parameters for basalt remain unpublished and were obtained from the source code.

strength/damage model described by Collins et al. (Collins et al. 2004) that incorporates a pressure-dependent melting curve (Senft & Stewart 2009) and frictional heating along cracks (Schultz & Crawford 2016) that leads to thermal softening (Crawford & Schultz 2013). BDL models the strength of the damaged material Y_d as

$$Y_d = f_d P_{\text{eff}}, \tag{A8}$$

where f_d is the coefficient of internal friction of the damaged material and P_{eff} is the effective pressure. All CTH simulations are in the strength-dominated regime, so no gravitational acceleration is considered.

A.3. iSALE

The ROCK model in iSALE (Collins et al. 2004) is a pressure- and damage-dependent strength model that describes the behavior of rock-like materials. ROCK is a more complex model than those of Drucker–Prager or Lund (see Raducan et al. 2019), in which strength is reduced as strain accumulates.

Table 8
iSALE Material Model Parameters

Description	Impactor	Strong target	Weak target
Material	Aluminum	SiO$_2$	
Equation of state	Tillotson[a]	ANEOS[b]	
Strength model	Johnson–Cook	ROCK	
ν, Poisson ratio	0.33	0.30	
ROCK strength parameters[c]			
Y_{s0}, yield strength at $P = 0$ (intact)	...	100 MPa	0.1 MPa
Y_{d0}, yield strength at $P = 0$ (damaged)	...	10 MPa	0.01 MPa
f_s, internal friction coefficient (intact)	...	1.2	
f_d, internal friction coefficient (damaged)	...	0.6	
$Y_{s\infty}$, yield strength at $P = \infty$ (intact)	...	3.5 GPa	
$Y_{d\infty}$, yield strength at $P = \infty$ (damaged)	...	1.5 GPa	
Ivanov damage parameters[d]			
ϵ_{fb}, minimum failure strain for low-pressure states	...	1×10^{-4}	
B, positive constant (increase in failure strain with pressure)	...	1×10^{-11}	
p_c, pressure above which failure is always compressional	...	3×10^{8}	
Johnson–Cook strength parameters[e]			
A, strain coefficient	244 MPa	...	...
B, strain coefficient	488 MPa	...	...
n, strain exponent	0.50	...	...
C, strain rate coefficient	0.02	...	...
m, thermal softening	1.70	...	...
Porosity model parameters[f]			
ϕ_0, initial porosity	...	30%	
α_0, initial distension	...	1.43	
α_x, distension at transition to power-law	...	1.00	
ϵ_E, elastic volumetric strain threshold	...	-1.88×10^{-4}	
κ, exponential compaction rate	...	0.90	

Notes.
[a] Tillotson (1962)
[b] Melosh (2007)
[c] Collins et al. (2004)
[d] Collins et al. (2004); Ivanov et al. (1997)
[e] Johnson & Cook (1983)
[f] Wünnemann et al. (2006)

The ROCK strength model defines the yield strength according to Equations (A3)–(A5), which were added to Spheral in order to better match the ROCK yield strength law in iSALE (see Table 8 for the numerical parameters used in this study). Note, however, that the damage in iSALE (which is a function of accumulated plastic strain) is defined differently than in Spheral.

The behavior of strength in rocks and soils is more complex than the strength in metals. In iSALE, a damage parameter, D, is used to define the extent of rock fracturing (Collins et al. 2004). This parameter varies between 0 for an intact, undamaged rock, to 1, for a completely fractured, damaged rock. Damaged rock has a much lower strength than intact rock. This work is using the Ivanov damage model, which prescribes the damage (D) as a function of plastic strain,

$$D = \min\left(\frac{\epsilon_p}{\epsilon_f}, 1\right), \quad (A9)$$

where ϵ_p is the invariant measure of the accumulated plastic strain and ϵ_f is the plastic strain at failure. In this model, ϵ_f is defined as a function of pressure,

$$\epsilon_f = \max\left(\epsilon_{fb}, B(p - p_c)\right), \quad (A10)$$

where ϵ_{fb} is a low minimum failure strain for low-pressure states and B and p_c are constants.

ORCID iDs

J. Michael Owen https://orcid.org/0000-0003-4796-124X
Mallory E. DeCoster https://orcid.org/0000-0002-1139-9235
Dawn M. Graninger https://orcid.org/0000-0003-1582-0581
Sabina D. Raducan https://orcid.org/0000-0002-7478-0148

References

Amsden, A. A., Ruppel, H. M., & Hirt, C. W. 1980, SALE: a simplified ALE computer program for fluid flow at all speeds, LA-8095, Los Alamos Scientific Lab. doi:10.2172/5176006
Arakawa, M., Saiki, T., Wada, K., et al. 2020, Sci, 368, 67
Barnes, J., & Lyon, S. 1988, SESAME equation of state Tech. Rep., No. 7530, Los Alamos National Lab.
Barnouin, O. S., Daly, M. G., Palmer, E. E., et al. 2019, NatGe, 12, 247
Benz, W., & Asphaug, E. 1994, Icar, 107, 98
Benz, W., & Asphaug, E. 1995, CoPhC, 87, 253
Britt, D. T., Yeomans, D., Housen, K., & Consolmagno, G. 2002, in Asteroids III, ed. W. F. Bottke, Jr. et al. (Tucson, AZ: Univ. of Arizona Press), 485
Bruck Syal, M., Michael Owen, J., & Miller, P. L. 2016, Icar, 269, 50
Campbell, J. 1998, PhD thesis, Cranfield Univ.

Cheng, A. F., Rivkin, A. S., Michel, P., et al. 2018, P&SS, 157, 104
Collins, G. S., Melosh, H. J., & Ivanov, B. A. 2004, M&PS, 39, 217
Collins, G. S., Melosh, H. J., & Wünnemann, K. 2011, IJIE, 38, 434
Crawford, D. 1999, 15th US Army Symp. on Solid Mechanics, SAND99-1118C, Sandia National Lab., https://www.osti.gov/biblio/7235
Crawford, D. A. 2020, IJIE, 137, 103464
Crawford, D. A., & Schultz, P. H. 2013, LPI Contribution, 1737, 3047
De León, J., Licandro, J., Serra-Ricart, M., Pinilla-Alonso, N., & Campins, H. 2010, A&A, 517, A23
Dotto, E., Della Corte, V., Amoroso, M., et al. 2021, P&SS, 199, 105185
Fritsch, F. N. 2016, LIP: The Livermore Interpolation Package, Version 1.6, Tech. Rep. LLNL-TR-406719-REV-5, Lawrence Livermore National Lab., doi:10.2172/1234602
Graninger, D., Bruck Syal, M., Owen, J. M., & Miller, P. L. 2018, AGUFM, P51A–11
Heberling, T., Terrones, G., & Weseloh, W. 2018, IJIE, 122, 1
Hermalyn, B., Schultz, P. H., Shirley, M., Ennico, K., & Colaprete, A. 2012, Icar, 218, 654
Hertel, E., Bell, R., Elrick, M., et al. 1993, Shock Waves at Marseille: Proceedings of the 19th International Symposium on Shock Waves (Berlin: Springer)
Holsapple, K. A., & Housen, K. R. 2007, Icar, 187, 345
Housen, K. R., & Holsapple, K. A. 2012, LPSC, 43, 2539
Ikeda, M., Tanaka, M., Yokoo, D., Koura, T., & Akahoshi, Y. 2017, Procedia Engineering, 204, 138
Ivanov, B. A., Deniem, D., & Neukum, G. 1997, IJIE, 20, 411
Johnson, G. R., & Cook, W. H. 1983, in Proc. of the 7th Int. Symp. on Ballistics (The Hague), 541
Johnson, J. D. 1994, Symp. on Thermophysical Properties (Boulder, CO: USDOE)
Jutzi, M., & Michel, P. 2014, Icar, 229, 247
Jutzi, M., Michel, P., Hiraoka, K., Nakamura, A. M., & Benz, W. 2009, Icar, 201, 802
Korycansky, D. G., Plesko, C. S., Jutzi, M., Asphaug, E., & Colaprete, A. 2009, M&PS, 44, 603
Lauretta, D. S., Balram-Knutson, S. S., Beshore, E., et al. 2017, SSRv, 212, 925

Lundborg, N. 1967, International Journal of Rock Mechanics and Mining Sciences & Geomechanics Abstracts, 4, 269
McGlaun, J. M., Thompson, S. L., & Elrick, M. G. 1990, IJIE, 10, 351
Melosh, H. J. 1989, Impact Cratering: A Geologic Process (Oxford: Clarendon Press)
Melosh, H. J. 2007, Metic & Planetary Science Archives, 42, 2079
Michel, P., Kueppers, M., Sierks, H., et al. 2018, AdSpR, 62, 2261
Naidu, S. P., Benner, L. A., Brozovic, M., et al. 2020, Icar, 348, 113777
Owen, J. M. 2010, in Proc. of the 5th Int. SPHERIC SPH Workshop Manchester, UK, 297
Owen, J. M. 2014, IJNMF, 75, 749
Owen, J. M., Villumsen, J. V., Shapiro, P. R., & Martel, H. 1998, ApJS, 116, 155
Raducan, S., Jutzi, M., Davison, T., et al. 2022, IJIE, 162, 104147
Raducan, S. D., Davison, T. M., & Collins, G. S. 2020, P&SS, 180, 104756
Raducan, S. D., Davison, T. M., Luther, R., & Collins, G. S. 2019, Icar, 329, 282
Rivkin, A. S., Chabot, N. L., Stickle, A. M., et al. 2021, PSJ, 2, 173
Schultz, P. H., & Crawford, D. A. 2016, Natur, 535, 391
Senft, L. E., & Stewart, S. T. 2009, E&PSL, 287, 471
Shuvalov, V. V., & Trubetskaya, I. A. 2008, SoSyR, 42, 1
Steinberg, D. J., & Lund, C. M. 1989, JAP, 651, 1528
Stickle, A., Rainey, E., Syal, M. B., et al. 2017, Procedia Engineering, 204, 116
Stickle, A. M., Atchison, J. A., Barnouin, O. S., et al. 2015, Procedia Engineering, 103, 577
Stickle, A. M., Bruck Syal, M., Cheng, A. F., et al. 2020, Icar, 338, 113446
Taylor, P. A. 1992, CTH Reference Manual : The Steinberg-Guinan- Lund Viscoplastic Model, Tech. Rep., Sandia National Lab.
Thompson, S. L., & Lauson, H. S. 1972, Improvements in the CHART D radiation-hydrodynamic code III: revised analytic equations of state, Tech. Rep. SC-RR-71-0714, Sandia National Lab.
Thompson, S. L., Lauson, H. S., Melosh, H. J., Collins, G. S., & Stewart, S. T. 2019, M-ANEOS: A Semi-Analytical Equation of State Code, 1.0, Zenodo, doi:10.5281/zenodo.3525030
Tillotson, H. J. 1962, Metallic Equations of State for Hypervelocity Impacts, General Atomic Report GA-3216, General Dynamics San Diego CA General Atomic Division, 141
Wünnemann, K., Collins, G. S., & Melosh, H. J. 2006, Icar, 180, 514